Exchange Bias between van der Waals Materials: Tilted Magnetic States and Field-Free Spin-Orbit-Torque Switching

CNF Project Number: 598-96
Principal Investigator: Daniel C. Ralph
User(s): Thow Min Jerald Cham

Affiliation(s): Laboratory of Atomic and Solid State Physics, Cornell University

Primary Source(s) of Research Funding: National Science Foundation/Division of Materials Research, Air Force Office of Scientific Research, Agency for Science Technology and Research (Singapore)

Contact: dcr14@cornell.edu, tc676@cornell.edu

Primary CNF Tools Used: Supra SEM, Nabity Nanometer Pattern Generator, AJA Sputter Deposition, Odd hour evaporator, Angstrom evaporator

Abstract:

Magnetic van der Waals heterostructures provide a unique platform to study magnetism and spintronics device concepts in the two-dimensional limit. Here, we report studies of exchange bias from the van der Waals antiferromagnet CrSBr acting on the van der Waals ferromagnet Fe_3GeTe_2 (FGT). The orientation of the exchange bias is along the in-plane easy axis of CrSBr, perpendicular to the out-of-plane anisotropy of the FGT, inducing a strongly tilted magnetic configuration in the FGT. Furthermore, the in-plane exchange bias provides sufficient symmetry breaking to allow deterministic spin-orbit torque switching of the FGT in CrSBr/FGT/Pt samples at zero applied magnetic field [1].

Summary of Research:

We study the interaction between ferromagnetic Fe_3GeTe_2 (FGT) [2] with perpendicular magnetic anisotropy (PMA) and antiferromagnetic CrSBr [3] with in-plane easy-axis anisotropy, and find that the interaction induces an in-plane exchange bias on the FGT. Since the exchange bias is an interface interaction and the anisotropy in FGT arises from a bulk mechanism, we conclude that the tilting is non-uniform through the thickness of FGT (illustrated schematically in Figure 1a).

We have also investigated whether the exchange interaction from the CrSBr can provide a sufficient symmetry-breaking field to allow for deterministic SOT switching in CrSBr/FGT/Pt heterostructures. In general, to achieve deterministic switching of a magnetic layer with PMA using SOT from a high-symmetry material like Pt requires an external symmetry-breaking field. We perform pulsed-current measurements with different fixed Bext, and after each pulse we measure the Hall voltage near zero current.

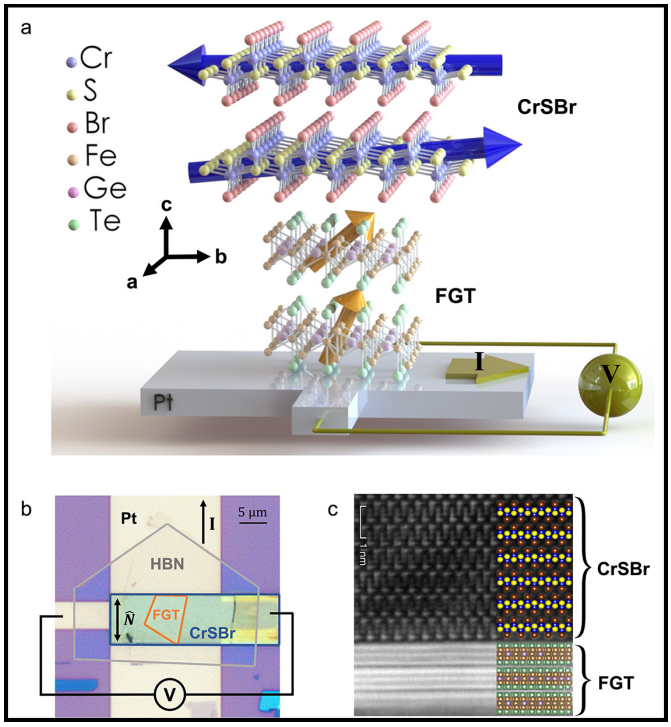

Figure 1: Device schematic and crystal structure (a) Schematic of a CrSBr/FGT het.erostructure dry transferred onto a Pt channel for spin-orbit torque pulse current switching measurements. (b) Top-view optical image of the CrSBr(30 nm)/FGT(9 nm)/Pt (10 nm) device with the b crystal axis of the CrSBr layer oriented parallel to the current (so that N^ ∥ I). (c) High angle annular dark field (HAADF) STEM cross-sectional image of the vdW interface of a different CrSBr/FGT heterostructure.

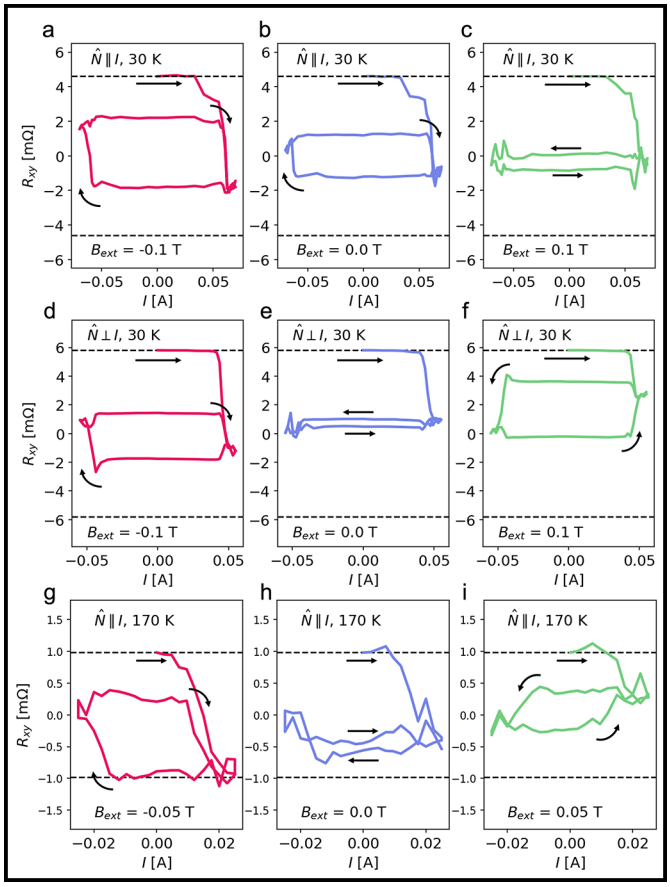

Figure 2: Pulsed-current-switching hysteresis loops of CrSBr/FGT/Pt samples. (a-c) Pulsed-current-switching hysteresis loops at 30 K for the sample with N^ ∥ I. The uniaxial exchange bias field enables deterministic spin-orbit-torque switching within the FGT layer at 0 T (panel (b)). (c) With a positive field of 0.1 T, the magnetization reversal hysteresis is quenched. (d-f) Pulsed-current switching hysteresis loops at 30 K for the sample with N^ ⊥ I. (g-i) Pulsed-current-switching hysteresis loops at 170 K, for the device with N^ ∥ I.

Figures 2a-c show the resulting switching loops for the device with $N^ \parallel I$ at 30 K. We observe deterministic switching (Figure 2b) for B_{ext} = 0 T, with the same switching chirality as when B_{ext} = -0.1 T (Figure 2a). When B_{ext} = 0.1 T, we see a quenching of the hysteresis (Figure 2c). In comparison, in the device for which $N^ \perp I$, there is negligible hysteresis at 0 T (Figure 2e) and the chirality of the magnetization reversal is opposite for ± 0.1 T (Figure 2d,f). When the temperature is raised above T_N to 170 K in the device with $N^ \parallel I$, we see no switching at 0 T (Figure 2h) and opposite switching chiralities at ± 0.05 T (Figure 2g,i). These findings indicate that a net exchange bias is induced parallel to the Néel vector of CrSBr when the temperature is lowered below *T*N.

Conclusion and Future Steps:

In conclusion, we report measurements of an in-plane exchange bias from CrSBr acting perpendicular to the out-of-plane anisotropy of FGT, in a direction parallel to the in-plane anisotropy axis of CrSBr. This exchange field results in a strongly-tilted magnetic configuration within the FGT, and can serve as an in-plane symmetry-breaking field that enables field-free deterministic switching driven by SOT in CrSBr/FGT/Pt devices. Although the CrSBr in our samples is likely in a multidomain state, we can make a rough estimate of the exchange bias strength from the external magnetic field required to cancel the exchange field and eliminate the deterministic switching. We estimate values as large as 0.15 T at low temperature, decreasing gradually with increasing temperature up to the T_N of CrSBr. A CrSBr thickness greater than ≈ 10 nm is required to provide exchange bias for switching at 30 K. This work opens possibilities for exploiting unique characteristics of vdW magnets and heterostructures to enable new functionality in spintronics.

References:

[1] Thow Min Jerald Cham, Reiley J Dorrian, Xiyue S Zhang, Avalon H Dismukes, Daniel G Chica, Andrew F May, Xavier Roy, David A Muller, Daniel C Ralph, and Yun.qiu Kelly Luo. Exchange bias between van der waals materials: tilted magnetic states and field-free spin-orbit-torque switching. arXiv preprint arXiv:2306.02129, 2023.

[2] Cheng Tan, Jinhwan Lee, Soon-Gil Jung, Tuson Park, Sultan Albarakati, James Partridge, Matthew R Field, Dougal G McCulloch, Lan Wang, and Changgu Lee. Hard magnetic properties in nanoflake van der waals fe3gete2. Nat. Commun., 9(1):1554, 2018.

[3] Evan J. Telford, Avalon H. Dismukes, Kihong Lee, Minghao Cheng, Andrew Wieteska, Amymarie K. Bartholomew, Yu-Sheng Chen, Xiaodong Xu, Abhay N. Pasupathy, Xiaoyang Zhu, Cory R. Dean, and Xavier Roy. Layered antiferromagnetism induces large negative magnetoresistance in the van der waals semiconductor CrSBr. Ad.vanced Materials, 32(37):2003240, 2020.

Physics of nm-Scale Superconductors and Magnets

CNF Project Number: 598-96
Principal Investigator(s): Daniel C. Ralph
User(s): Xiaoxi Huang

Affiliation(s): Department of Physics, Cornell University

Primary Source(s) of Research Funding: Semiconductor Research Corporation-
Superior Energy-efficient Materials and Devices

Contact: dcr14@cornell.edu, xh384@cornell.edu

Primary CNF Tools Used: Heidelberg Mask Writer - DWL66FS, JEOL 6300, AJA Sputter Deposition

Abstract:

We have been actively using the Heidelberg Mask Writer - DWL66FS to make spin torque ferromagnetic resonance and second harmonic Hall devices for spin-orbit torque generation study. JEOL 6300 electron beam writer has been employed to make non-local devices for spin transport study.

Summary of Research:

In the past year, one of our research focuses is to study unconventional spin-orbit torque generation in exotic material systems, consisting of a spin-orbit coupled material and a ferromagnet. The ferromagnet serves as a sensitive spin detector, whose magnetization state is subject to the perturbation induced by spin current generated in the spin-orbit coupled material. Two different techniques were employed to study spin-orbit torque generation in these systems. Since the device dimension is in the order of microns (Figure 1a, b), a photolithography recipe is developed to fabricate those devices. To begin with, spin torque ferromagnetic resonance is the mostly commonly used technique to measure spin orbit torque generation. The device made with the Heidelberg Mask Writer - DWL66FS at Cornell NanoScale Facility is shown in Figure 1a. The device consists of a T shaped bar made of the target material systems and a symmetric Ground-Signal-Ground contact that produces no net Oersted field when the applied high frequency current travels through. Moreover, second harmonic Hall measurement is another technique that Ralph group has pioneered to measure spin-orbit torque generation. The second harmonic Hall measurements are performed on Hall devices (Figure 1b), with external magnetic field rotated in the device plane. To make the Hall devices, Hall bars with three Hall crosses are first exposed with DWL 66fs. Then an ion mill step is followed to remove the material that is not protected by the photoresist. Finally, a second step exposure is performed to align contacts to the Hall crosses. Contacts made of Pt are deposited in the AJA sputter system for both spin torque ferromagnetic resonance and second harmonic Hall devices.

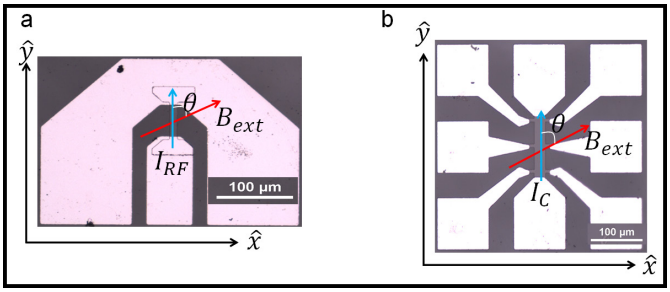

Figure 1: Devices for spin orbit torque generation study. a) Spin torque ferromagnetic resonance devices made with the Heidelberg Mask Writer - DWL66FS. b) Hall devices made with the DWL66FS. Mark alignments were used for the second step exposure.

The other project we have been actively working on at the Cornell NanoScale Facility is the non-local spin transport in magnetic materials. Magnetic materials such as ferrimagnets [1,2] and antiferromagnets [3,4] have been shown to have the capability of carrying spin information over long distance. To study spin transport in magnetic insulators, non-local devices shown in Figure 2 [5] consisting of an injection channel and a detection channel that are separated by various distances are made with electron beam lithography. To achieve sub-micron down to 200 nm of distances between the two channels, electron beam lithography tool JEOL 6300 is used to expose features as small as 200 nm.

Conclusions and Future Steps:

We have successfully measured spin-orbit torque generation in spin-orbit coupled materials and spin transport in magnetic insulator in the devices fabricated at the Cornell NanoScale Facility. Our future steps include: 1. Study spin-orbit torque generation in the same material with various orientations. 2. Study the distance dependence of spin transport in the magnetic insulators.

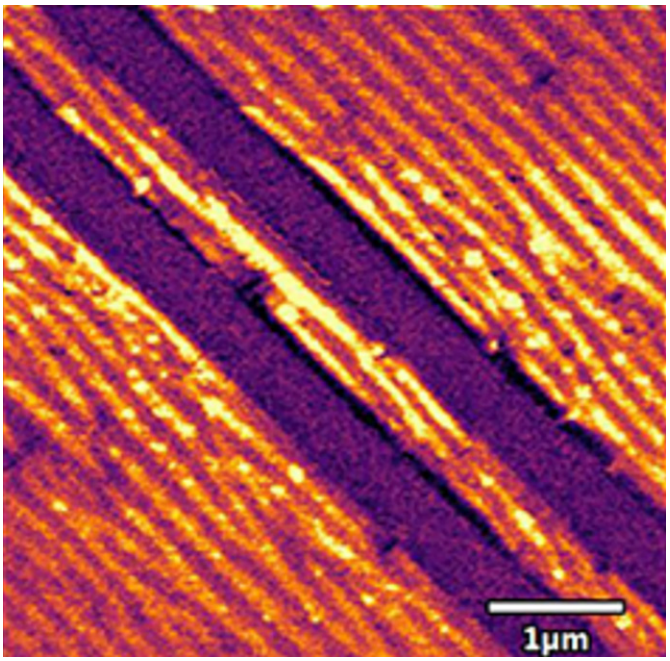

Figure 2: Non-local devices for long distance spin transport study. The channel width and spacing between two channels are 500 nm.

References:

[1] L. J. Cornelissen, J. Liu, R. A. Duine, J. Ben Youssef, and B. J. van Wees. "Long-distance transport of magnon spin information in a magnetic insulator at room temperature". Nat. Phys. 11, 1022(2015).

[2] X.-Y. Wei, O. Alves Santos, C. H. Sumba Lusero, G. E. W. Bauer, J. Ben Youssef, and B. J. van Wees. "Giant magnon spin conductivity in ultrathin yittrium iron garnet films". Nat. Mater. 21, 1352(2022).

[3] R. Lebrun, A. Ross, S. A. Bender, A. Qaiumzadeh, L. Baldrati, J. Cramer, A. Brataas, R. A. Duine, and M. Klaui. "Tunable long-distance spin transport in a crystalline antiferromagnetic iron oxide". Nature 561, 222(2018).

[4] Jiahao Han, Pengxiang Zhang, Zhen Bi, Yabin Fan, Taqiyyah S. Safi, Junxiang Xiang, Joseph Finley, Liang Fu, Ran Cheng, and Luqiao Liu. "Birefringence-like spin transport via linearly polarized antiferromagnetic magnons". Nat. Nanotechnol. 15, 563(2020).

[5] Xiaoxi Huang et al. "Manipulating chiral-spin transport with ferroelectric polarization". https://arxiv.org/abs/2306.02185.

Thermally-Generated Spin Current in the Topological Insulator Bi_2Se_3

CNF Project Number: 598-96
Principal Investigator(s): Daniel C. Ralph
User(s): Rakshit Jain

Affiliation(s): Physics Department, Cornell University
Primary Source(s) of Research Funding: Department of Energy, National Science Foundation
Contact: dcr14@cornell.edu, rj372@cornell.edu
Primary CNF Tools Used: AJA sputter deposition, 5X g-line stepper

Abstract:

We present measurements of thermally-generated transverse spin currents in the topological insulator Bi2Se3, thereby completing measurements of interconversions among the full triad of thermal gradients, charge currents, and spin currents. We accomplish this by comparing the spin Nernst magneto-thermopower to the spin Hall magnetosistance for bilayers of Bi_2Se_3/CoFeB. We find that Bi_2Se_3 does generate substantial thermally-driven spin currents. A lower bound for the ratio of spin current density to thermal gradient is shown in Equation (A) at right, and a lower bound for the magnitude of the spin Nernst ratio is -0.61 ± 0.11. The spin Nernst ratio for Bi_2Se_3 is the largest among all materials measured to date, 2-3 times larger compared to previous measurements for the heavy metals Pt and W.

$$\frac{J_s}{\nabla_x T} = (4.9 \pm 0.9) \times 10^6 \left(\frac{\hbar}{2e}\right) \frac{Am^{-2}}{K\mu m^{-1}} \quad \textbf{(A)}$$

$$J_s = \frac{\hbar}{2e}\frac{\theta_{SH}}{\rho_{SS}}E. \quad \textbf{(1)}$$

$$\Delta R(\hat{m}) = (1 - m_y^2)\Delta R_{SMR} = \Delta R_{SMR} cos^2\theta \quad \textbf{(2)}$$

$$J_s = -\frac{\hbar}{2e}\frac{\theta_{SN}}{\rho_{SS}} S_{SS} \nabla_x T. \quad \textbf{(3)}$$

$$\Delta V_{th}^x = -l\nabla_x T(1 - m_y^2) S_{SNT} = -l\nabla_x T S_{SNT} cos^2\theta \quad \textbf{(4)}$$

Equations (A) through (4).

Summary of Research:

By taking advantage of the electron's spin as well as its charge, the field of spin caloritronics has provided new strategies for energy harvesting from thermal gradients, for thermal management within electronics, and for magnetic manipulation [1]. However, the field has been limited by low efficiencies for interconversion between thermal gradients and spin currents within the materials studied to date. Here, we provide measurements of the efficiency of transduction from a thermal gradient to spin current density in a topological insulator. Topological insulators have already been demonstrated to provide very high efficiencies for interconversion between the other two legs of the triad of thermal gradients, charge currents, and spin currents. Topological insulators have achieved record efficiencies for transduction between charge current density and spin current density that are of interest for applications in spin-orbit-torque manipulation of magnetic devices [2], and also highly-efficient transduction of thermal gradients to electric field with potential for thermoelectric applications [3]. We find that the topological insulator Bi_2Se_3 also enables highly-efficient transduction of thermal gradients to spin currents, with by far the largest spin Nernst ratio among materials measured to date.

We measure thermally-generated spin currents using the same physics by which electrically-generated spin currents give rise to the spin Hall magnetoresistance (SMR) effect [4]. In the electrically-generated case, an electric field E applied in the plane of a spin-source/ferromagnet bilayer gives rise to a vertically-flowing spin current density J_s via the spin Hall effect, with an efficiency characterized by the spin Hall ratio, θ_{SH} Equation (1) above, where $\hbar$ is the reduced Planck constant, e is the magnitude of the electron charge, and ϱ_{SS} is the electrical resistivity of the spin-source material. The degree of reflection of this spin current at the magnetic interface depends on the orientation of the magnetization $m\hat{}$ in the magnetic layer. The reflected spin current produces a voltage signal by the inverse spin Hall effect, causing the resistance of the bilayer to depend on the magnetization angle (4), which can be further simplified in geometry studied in this work (Figure 1 (A)), Equation (2).

Here m_y is the component of the magnetization unit vector that is in-plane and perpendicular to the electric field. Similarly, the thermally-generated spin current and voltages takes the form in Equations (3) and (4) where θ_{SN} is the spin Nernst ratio, S_{SS} is the Seebeck coefficeint

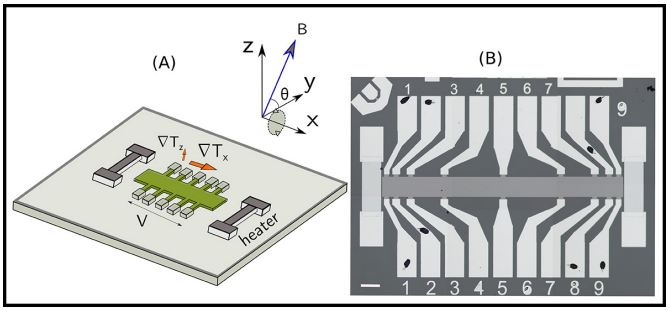

Figure 1: (A) Sample geometry for the spin Nernst magneto-thermopower experiments. (B) Microscope image of the device used for measuring spin Nernst magneto-thermopower. Scale bar is equivalent to 200 μm.

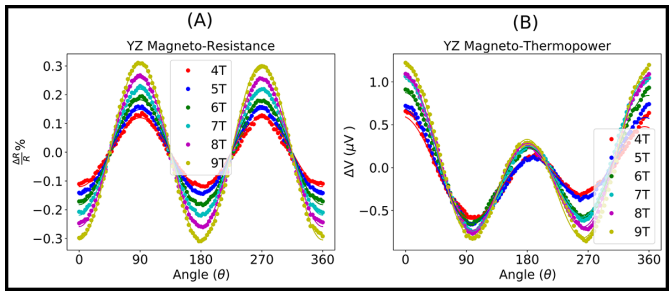

Figure 2: (A) Magnetoresistance percentage ratio $(\frac{\nabla R}{R} \times 100)$ as a function of the magnetic field angle and R magnitude for bilayers of Bi_2Se_3 (8 nm)/CoFeB (5 nm) at room temperature, for magnetic field rotated in the YZ plane. The four-point device resistance R = 2.137 kOhms. (B) YZ magneto-thermopower voltage as a function of the magnetic field angle and magnitude for the same sample. The heater power used for these sweeps was fixed at 442 mW (equivalent to a temperature drop of 6.8 K along the l = 1.8 mm length of the device).

of the spin source, S_{SNT} is the coefficient of the spin Nernst magneto-thermopower, which represents voltage arising from thermally generated spin currents, $\nabla_x T$ is the in-plane thermal gradient and l is the length of the device.

The results are plotted in Figure 2 for both electrically and thermally generated voltages. After accounting for field dependent magneto-resistance and magneto-thermopower arising from the Bi_2Se_3 (5) layer, we report, $100 \times \Delta R_{SMR}/R = 0.126 \pm 0.008$ where R is the resistance of the device and $S_{SNT} = 90 \pm 10\ nV/\kappa$. Using these values, we can estimate the ratio θ_{SN}/θ_{SH} = -0.83 ± 0.15 and θ_{SN} is approximately -0.61 ± 0.11.

These numbers can be used to estimate the net thermally generated spin currents as $J_s / \nabla_x T$ is $(4.9 \pm 0.9) \times 10^6$ $(\hbar/2e)$A m^{-2} / κ μm^{-1}.

Conclusions:

In summary, by comparing measurements of the spin Nernst magneto-thermopower in Bi_2Se_3/CoFeB bilayers to the spin Hall magnetoresistance, we find a lower bound for the magnitude of the spin Nernst ratio for Bi_2Se_3 of -0.61 ± 0.11, roughly three times greater than that of previously measured values for Pt and 2-3 times greater than that of W. Moreover, the net spin current generated per unit thermal gradient $J_s/\Delta T_x$ is higher in Bi_2Se_3 than for W and of a similar magnitude as Pt despite the higher resistivity of Bi_2Se_3.

References:

[1] Bauer, G. E., Saitoh, E., and Van Wees, B. J. Spin caloritronics. Nature Materials 11, 391-399 (2012).

[2] Mellnik, A., et al. Spin-transfer torque generated by a topological insulator. Nature 511, 449-451 (2014).

[3] Hor, Y., et al. p-type Bi_2Se_3 for topological insulator and low-temperature thermoelectric applications. Physical Review B 79, 195208 (2009).

[4] Nakayama, H., et al. Spin Hall magnetoresistance induced by a nonequilibrium proximity effect. Physical Review Letters 110, 206601 (2013).

[5] Jain, R., et al. Thermally-generated spin current in the topological insulator Bi_2Se_3. arXiv preprint arXiv:2210.05636 (2022).

Fabricating Micron-Sized Skyrmion-Spintronic Devices

CNF Project Number: 598-96
Principal Investigator(s): Daniel C. Ralph
User(s): Maciej Olszewski

Affiliation(s): Laboratory of Atomic and Solid State Physics (LASSP), Cornell University

Primary Source(s) of Research Funding: Defense Advanced Research Projects Agency (DARPA), National Science Foundation (NSF)

Contact: dcr14@cornell.edu, mwo34@cornell.edu

Website(s): https://ralphgroup.lassp.cornell.edu/

Primary CNF Tools Used: GCA 6300 DSW 5X g-line Wafer Stepper, GCA AutoStep 200 DSW i-line Wafer Stepper, Heidelberg Mask Writer - DWL2000, AJA Ion Mill, AJA Sputter Deposition, YES Asher, DISCO Dicing Saw

Abstract:

Magnetic skyrmions are a candidate for next-generation spintronic devices. Their topological nature makes them robust, allowing for a non-volatile, high-speed, and low-power-consumption method of storing and processing information. In addition, recent advances in skyrmionics have demonstrated both electrical and thermal techniques for controlling skyrmion densities in thin films. Here, we present initial measurements of magnetic resonance in ferromagnetic multilayers with interfacial Dzyaloshinskii-Moriya interaction. We have performed room temperature experiments utilizing both conventional field-driven ferromagnetic resonance and spin-torque ferromagnetic resonance. We find a difference in the resonance readout between the phases with and without skyrmions but are yet to find direct evidence for resonance readout of skyrmions themselves. Our work is further supported by Lorentz transmission electron microscopy with spatial resolution on the order of a few nanometers, where we directly observe skyrmions in our thin films.

Summary of Research:

Conventional spin-torque ferromagnetic resonance (ST-FMR) devices consist of two layers, one heavy metal (HM) spin Hall layer and one ferromagnet (FM) with in-plane anisotropy [1]. As current passes through the HM layer a spin current is generated in the direction perpendicular to the current direction. The generated spin current then proceeds into the FM layer and exerts a torque on the magnetization. If alternating current is passed, the spin current generated will also be alternating, and under certain conditions the spin torque can cause the FM to resonate. The resonance of the magnet can be captured with the changes in the magnetoresistance of the device. Further, the resonances can be fitted to extract various parameters, such as the strength of the torques, magnetic damping, and effective magnetization.

Skyrmions, topologically protected spin textures, present a novel and robust system for resonance-based spintronic devices. They can be found in a variety of systems, including thin ferromagnetic films with the presence of the Dzyaloshinskii-Moriya interaction and broken inversion symmetry [2]. Due to their topological nature, skyrmions are stable under small perturbations from defects and other external fluctuations, making them a great candidate for various memory-based applications. Further, it has been demonstrated that skyrmions can be observed via the topological Hall effect and their density can be controlled with current pulses [3].

The main goal of our work is to incorporate thin films which host skyrmions into ST-FMR devices to directly measure skyrmion resonances and control their density to increase or decrease the resonance readout. We grow our skyrmion multilayers, consisting of platinum, cobalt, and ruthenium on a sapphire substrate, using our own AJA magnetron sputtering tool. After depositing the films, we perform one round of photolithography on either the g-line or i-line stepper to outline the shape of the devices and use the AJA ion mill to mill our film to the proper device size. Next, we do either one or two rounds of photolithography for writing the contacts for the devices. Finally, we use the AJA sputter to deposit titanium and platinum to make proper electrical connection to the devices. This process usually yields very consistent results with device fabrication, and we can fabricate

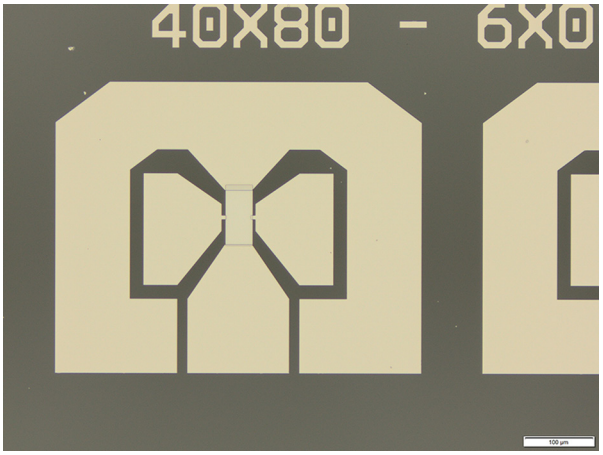

Figure 1: An image of fabricated thin film devices with contacts on a sapphire substrate.

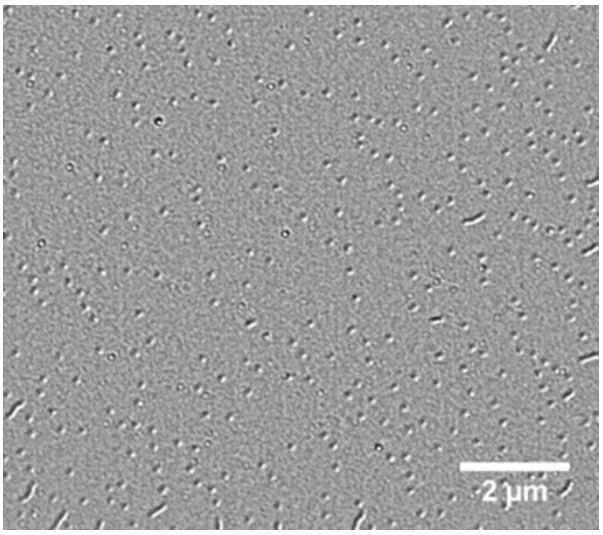

Figure 2: A Lorentz transmission electron microscopy scan of out thin film showing the density and size of the skyrmions.

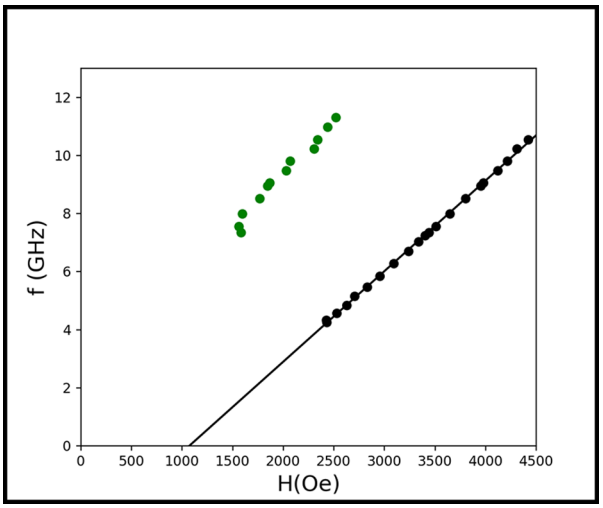

Figure 3: Positions of the magnetic resonances of the skyrmion film as a function of frequency and magnetic field.

around 100 devices of different shapes and sizes during this procedure, an example of which is shown in Figure 1.

We can directly observe if skyrmions are present in our samples by conducting Lorentz transmission electron microscopy (L-TEM) and looking at the changes in the reflections of the transmitted electrons, as shown in Figure 2. After, ensuring that we have skyrmions present, we conduct standard ST-FMR measurements as a function of the frequency of the current applied and the strength of the external magnetic field. In Figure 3, we show the positions of the resonance peaks as a function of frequency and magnetic field. Unfortunately, our preliminary work does not show any resonances in the regions where skyrmions are present, based on the L-TEM scans. We are continuing our efforts to find skyrmion resonance by considering other device geometries and slight changes to the thin films.

References:

[1] Karimeddiny, et al., Phys. Rev. Applied 14, 024024 (2020).
[2] Fert, et al., Nature Review Materials, 2, 17031 (2017).
[3] Park, et al., Journal of Applied Physics 128, 23 (2020).

Surface Acoustic Waves in Magnetic Materials

CNF Project Number: 598-96
Principal Investigator(s): Daniel C. Ralph
User(s): Yongjian Tang

Affiliation(s): Physics, Cornell University
Primary Source(s) of Research Funding: DE-SC0017671 Department of Energy
Contact: dcr14@cornell.edu, yt498@cornell.edu
Website(s): https://ralphgroup.lassp.cornell.edu
Primary CNF Tools Used: JEOL 6300, SC4500 evaporator, Zeiss Supra SEM, AJA sputter, 5X stepper

Abstract:

We have developed both photolithography and e-beam lithography recipes for interdigital transducers (IDTs) based on multiferroic $BiFeO_3$ (BFO) thin films. Using ultra-high-frequency lock-in (UHFLI) measurements, we successfully demonstrated the generation of surface acoustic waves (SAWs) in BFO epitaxial films. Pulse echo measurements and vector network analyzer are deployed to further characterize the properties of the SAWs.

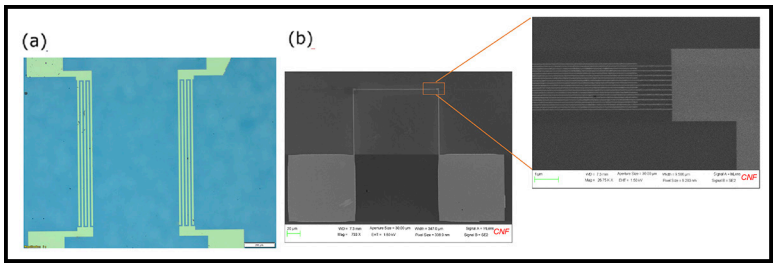

Figure 1: (a) Optical image of IDTs patterned by photolithography and (b) SEM image of IDTs patterned by e-beam lithography.

Summary of Research:

SAWs have been extensively used in electronic components which include delay lines, filters, transformers, etc., devices that are based on transduction from electric energy to mechanical energy in piezoelectric materials. Because SAWs can be easily generated and launched into elastic materials, they become a powerful tool for fundamental research in condensed matter physics, widely used to characterize, manipulate, and detect electrical and magnetic properties. For instance, mismatch of sound velocities in SAW substrate and fluidic medium is exploited to drive fluid actions such as pumping, mixing and jetting. Intrinsic parameters of a material can be obtained by measuring the speed and attenuation of SAWs. The combination of SAWs with magnetism gives rise to novel phenomena such as acoustically driven spin pumping, SAW-induced ferromagnetic resonance, magnetic domain motion as well as nonreciprocal SAW propagation, via magnon-phonon coupling. Dynamic strain field induced by SAWs allows manipulation of photoluminescence in low-dimensional materials.

BFO is a room temperature multiferroic where ferroelectricity, antiferromagnetism, and a weak spin-canted magnetization coexist. It would be interesting to investigate the coupling between these order parameters. Since all ferroelectric materials are intrinsically piezoelectric, SAWs are also expected to be generated in BFO. Via piezoelectric effect, an IDT converts electrical energy into mechanical energy that propagates at the surface in the form of surface acoustic waves. In this project, we aim to fabricate input and output IDTs to verify the generation of SAWs in BFO-based devices, which would open new possibilities to control, manipulate and detect the change in these order parameters.

The fabrication was done on a 100 nm thick BFO sample. 15 pairs of IDTs are patterned in a 10 mm by 10 mm square using 5X stepper. An IDT consists of two interlocking comb-shaped arrays of metal electrodes. The geometry of these electrodes determines the wavelength of the SAW. For the IDT shown in Figure 1(a), it has five fingers that span a distance range of 101.25 μm, which means the width of each finger is 11.25 μm, and the wavelength is four times that, 45 μm. As shown in Figure 1(b), we have also developed method for patterning IDTs using e-beam lithography. These IDTs can have extremely small wavelength (down to 20 nm) and hence gigahertzworking frequency range.

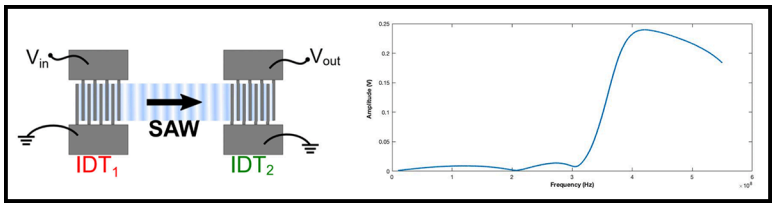

Figure 2: UHFLI measurement.

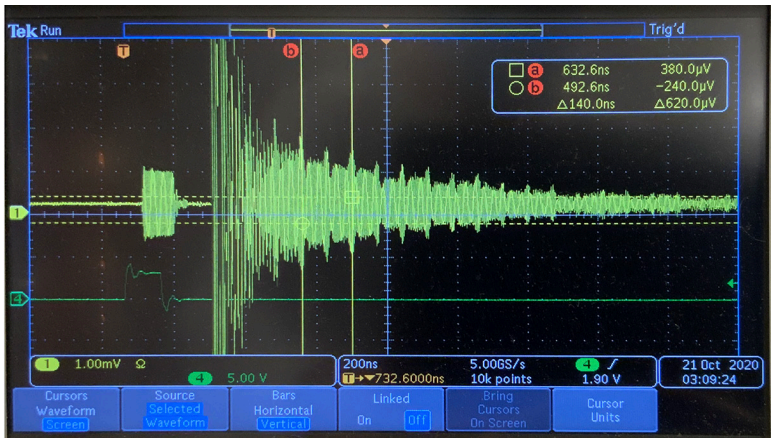

Figure 3: Pulse echo measurement.

UHFLI measurement was performed on the photolithographically defined IDTs (Figure 2). The amplitude of the voltage at output IDT is measured at different frequency with a fixed input voltage of 1 V. We observe a sharp increase of amplitude after 300 MHz and amplitude peaks at around 410 MHz. This indicates that in this range of frequency, SAWs are generated with highest efficiency. More SAWs are generated at these frequencies, and they propagate to the output IDT and are converted back into electric signal.

We also performed a pulse echo measurement on the same sample. For this measurement, we excited SAW at 410 MHz to generate as many SAWs as possible. The SAWs are bouncing back and forth between the IDTs and thus we observed echoes with an oscilloscope. Considering that the transmission at the IDTs, the echo signal will decay eventually. Ideally, we would like to see separated packs of signal with decreasing amplitude, but our echoes are overlapping making them hard to be distinguished. This can be solved by increasing the spatial separation between IDTs and shorted the pulse width. Still, we observe evenly spaced spiles, which also indicate the generation of SAWs. From the spacing between the echoes, we can calculate quantities such as SAW velocity, attenuation, etc.

Nanofabricated Superconducting Devices for Vortex Dynamics and Qubits

CNF Project Number: 1314-05
Principal Investigator(s): Britton L.T. Plourde
User(s): Brad Cole, Kenneth Dodge, Clayton Larson, Eric Yelton

Affiliation(s): Department of Physics, Syracuse University
Primary Source(s) of Research Funding: Army Research Office
Contact: bplourde@syr.edu, bgcole@syr.edu, krdodgej@syr.edu, cllarson@syr.edu, epyelton@syr.edu
Primary CNF Tools Used: ASML Photostepper, JEOL 6300, Plasma-Therm 770

Abstract:

We fabricate superconducting microwave devices for studying the dynamics of vortices at low temperatures and for forming novel qubits. Vortices are quantized bundles of magnetic flux that thread many different superconductors over a particular range of applied magnetic field. By using disordered superconducting thin films to form high kinetic inductance wires combined with novel arrays of Josephson junctions, we are able to build structures that can lead to qubits that are topologically protected against decoherence. With charge-sensitive superconducting qubits, we are able to probe sources of correlated errors in quantum processors.

Summary of Research:

Superconducting microwave circuits play an important role in quantum information processing. Circuits composed of Josephson junctions and capacitors with superconducting electrodes can serve as qubits, the fundamental element of a quantum computing architecture. Various loss mechanisms limit the ultimate performance of these devices, including trapped magnetic flux vortices. Vortices can be trapped in the superconducting electrodes when background magnetic fields are present and contribute dissipation when driven with microwave currents [1]. Thus, techniques for controlling the trapping of vortices are critical to the development of large-scale quantum information processors with superconducting circuits.

By arranging nanoscale Al-AlOx-Al Josephson tunnel junctions in novel arrays, it is possible to implement new qubit designs that are protected against decoherence [2-4]. We are also able to use such Al-AlOx-Al tunnel junctions in superconducting qubits to probe poisoning effects from nonequilibrium quasiparticles, which are a source of correlated errors in quantum processors. We can mitigate this quasiparticle poisoning through the use of electroplated Cu metallic reservoirs for downconversion of high energy phonons [5].

We fabricate our microwave resonators from various superconducting films, including aluminum and niobium, deposited onto silicon wafers in vacuum systems at Syracuse University. We define the patterns on the ASML stepper and transfer them into the films with a combination of reactive ion etching and liftoff processing. For defining Josephson junctions, we use the JEOL 6300 along with a dedicated deposition system at Syracuse University. We measure these circuits at temperatures of 100 mK and below in our lab at Syracuse University.

References:

[1] Song, C., Heitmann, T.W., DeFeo, M.P., Yu, K., McDermott, R., Neeley, M., Martinis, John M., Plourde, B.L.T.; "Microwave response of vortices in superconducting thin films of Re and Al"; Physical Review B 79, 174512 (2009).

[2] Doucot, B., Ioffe, L.; "Physical implementation of protected qubits"; Reports on Progress in Physics75, 072001 (2012).

[3] Liu, Y., Dodge, K., Cole, B., Shearrow, A., Brann, E., Snyder, M., Klots, A., Ioffe, L., McDermott, R., Plourde, B.; "Quantum stabilizers implemented with superconducting hardware"; Bull. Am. Phys. Soc. 2023, https://meetings.aps.org/Meeting/MAR23/Session/M75.3

[4] Dodge, K., Liu, Y., Klots, A., Cole, B., Shearrow, A., Senatore, M., Zhu, S., Ioffe, L., McDermott, R., Plourde, B.; "Hardware implementation of quantum stabilizers in superconducting circuits"; arXiv:2303.00625.

[5] Iaia, V., Ku, J., Ballard, A., Larson, C.P., Yelton, E., Liu, C.H., Patel, S., McDermott, R., Plourde, B.L.T.; "Phonon downconversion to suppress correlated errors in superconducting qubits"; NatureCommunications 13, 6425 (2022).

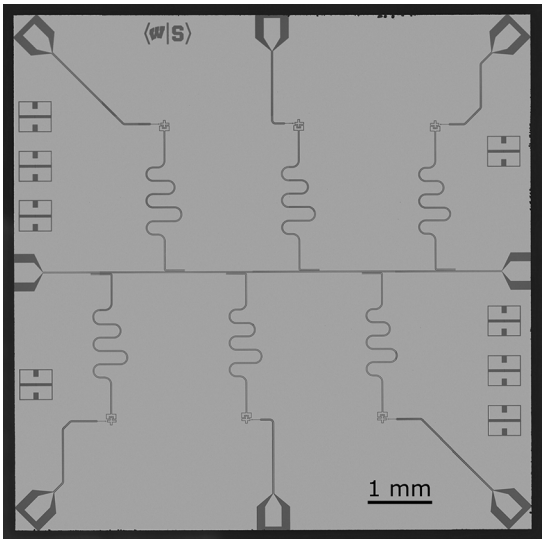

Figure 1: Optical micrograph of multi-qubit chip with Nb base layer and Al-AlOx-Al tunnel junctions for probing phonon-mediated correlated errors.

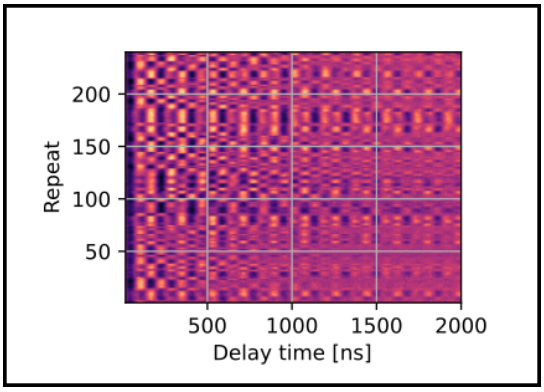

Figure 2: Repeated measurements of Ramsey fringe oscillations for charge-sensitive superconducting qubit subject to random offset charge jumps due to high energy particle impacts on device.

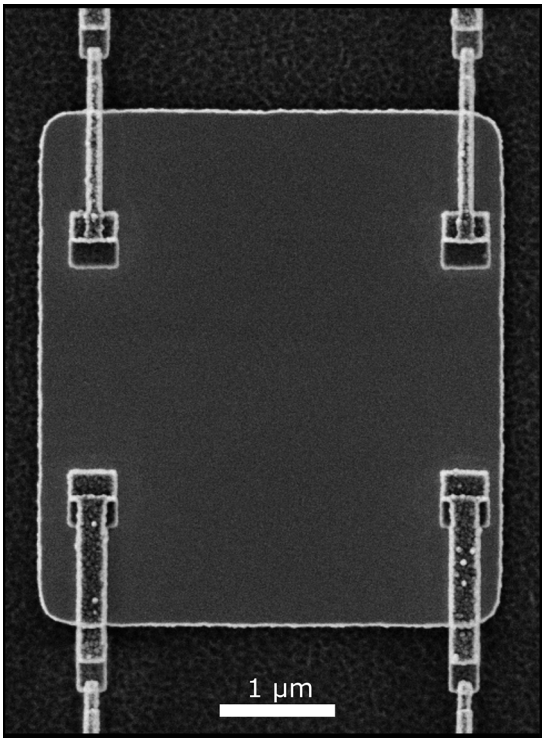

Figure 3: SEM image of central superconducting Nb island connected to four Al-AlOx-Al tunnel junctions for topologically protected superconducting circuit.

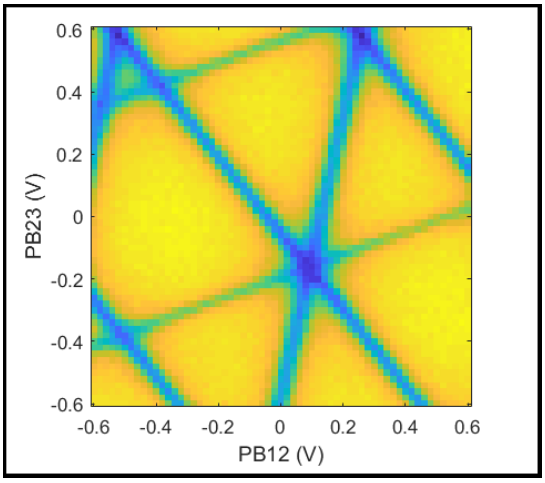

Figure 4: Measurement of microwave readout cavity modulation with magnetic flux using on-chip control lines coupled to topologically protected superconducting circuit.

Fabrication of Nanoscale Josephson Junctions for Quantum Coherent Superconducting Circuits

CNF Project Number: 1735-08
Principal Investigator(s): Britton L.T. Plourde
User(s): Brad Cole, Tianna McBroom, JT Paustian

Affiliation(s): Department of Physics, Syracuse University
Primary Source(s) of Research Funding: Air Force Research Lab, Air Force Office of Scientific Research
Contact: bplourde@syr.edu, bgcole@syr.edu, tamcbroo@syr.edu, jtpausti@syr.edu
Primary CNF Tools Used: ASML Photostepper, JEOL 6300, Plasma-Therm 770

Abstract:

We fabricate nanoscale superconductor tunnel junctions and other structures for experiments involving quantum coherent circuits. Such circuits have shown great promise in recent years for explorations of quantum mechanics at the scale of circuits on a chip and for forming qubits, the foundational elements of a quantum computer. The quantum state of these superconducting qubits can be manipulated with microwave radiation at low temperatures. We are currently developing superconducting metamaterial structures with novel microwave mode spectra for coupling to superconducting qubits.

Summary of Research:

The unique properties of nanoscale Josephson junctions enable a wide range of novel superconducting circuits for investigations in many diverse areas. In recent years, circuits composed of such junctions have emerged as promising candidates for the element of a quantum computer, due to the low intrinsic dissipation from the superconducting electrodes and the possibility of scaling to many such qubits on a chip [1]. The quantum coherent properties of the circuits are measured at temperatures below 50 mK with manipulation of the qubit state through microwave excitation.

We are developing multimode microwave resonators using combinations of superconducting lumped-circuit elements to engineer metamaterial transmission lines, including metamaterial ring resonator devices. These structures exhibit novel mode structures characteristic of left-handed materials [2]. We are fabricating such metamaterial transmission lines from Al and Nb films on Si and characterizing these at low temperatures [2]. We are working on experiments to couple these left-handed lines and ring resonators to superconducting qubits for experiments involving the exchange of microwave photons [2-4].

We pattern these circuits at the CNF with nanoscale structures defined with electron-beam lithography on the JEOL 6300 integrated with photolithographically defined large-scale features. The junctions are fabricated using the standard double-angle shadow evaporation technique, in which a resist bilayer of copolymer and PMMA is used to produce a narrow PMMA airbridge suspended above the substrate. Evaporation of aluminum from two different angles with an oxidation step in between forms a small Al-AlOx-Al tunnel junction from the deposition shadow of the airbridge. We have developed a process for defining these junctions with electron-beam lithography and we perform the aluminum evaporations in a dedicated chamber at Syracuse. We pattern large-scale features using the ASML stepper, with electron-beam evaporation of Al and sputter-deposition of Nb. Measurements of these circuits are performed in cryogenic systems at Syracuse University, including dilution refrigerators for achieving temperatures below 30 mK.

References:

[1] Clarke, J. and Wilhelm, F.K.; "Superconducting quantum bits"; Nature, 453, 1031 (2008).
[2] Wang, H., Zhuravel, A., Indrajeet, S., Taketani, B., Hutchings, M., Hao, Y., Rouxinol, F., Wilhelm,F., LaHaye, M.D., Ustinov, A., Plourde, B.; "Mode Structure in Superconducting Metamaterial Transmission Line Resonators"; Physical Review Applied 11, 054062 (2019).
[3] Indrajeet, S., Wang, H., Hutchings, M.D., Taketani, B.G., Wilhelm, F.K., LaHaye, M.D., Plourde, B.L.T.; "Coupling a Superconducting Qubit to a Left-Handed Metamaterial Resonator"; Physical Review Applied 14, 064033 (2020).
[4] McBroom, T.A., Schlabes, A., Xu, X., Ku, J., Cole, B.G., Ansari, M., Plourde, B.; "Multimode entangling interactions between transmons coupled through a metamaterial ring-resonator: experiment"; Bull. Am. Phys. Soc. 2023, https://meetings.aps.org/Meeting/MAR23/Session/A73.7.

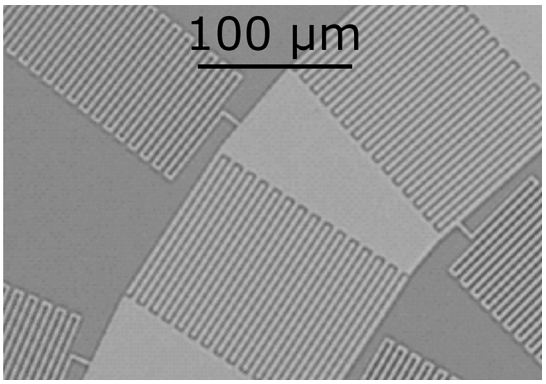

Figure 1: Optical micrograph of unit cell of left-handed metamaterial ring resonator fabricated from Nb on Si with interdigitated capacitor and meander-line inductors.

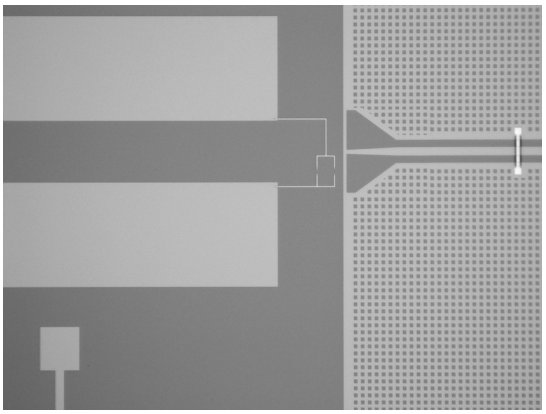

Figure 2: Zoomed-in optical micrograph of transmon qubit with Al-AlOx-Al junctions and Nb capacitor pads coupled to metamaterial ring resonator with on-chip Nb flux-bias line.

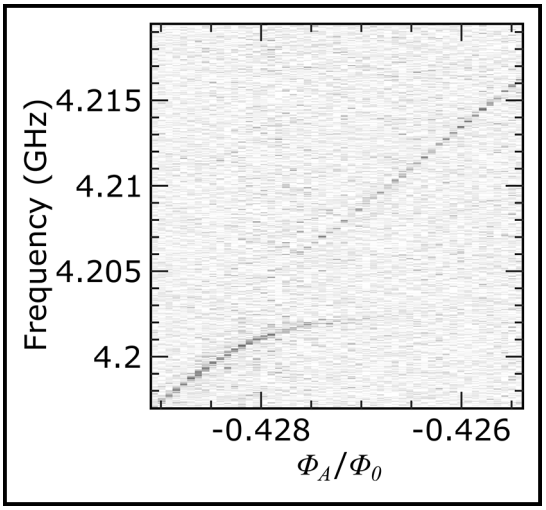

Figure 3: Measurement of qubit spectroscopy on metamaterial ring resonator with two qubits while tuning magnetic flux bias of one qubit. Splitting feature corresponds to exchange coupling between qubits when bare frequency of qubit being tuned approaches resonance with second qubit.

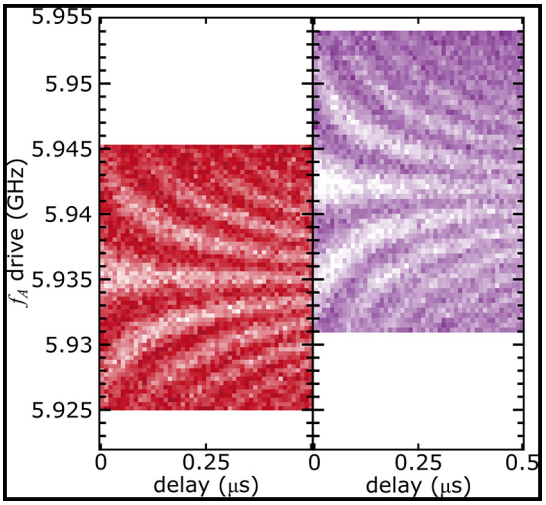

Figure 4: Measurement of Ramsey fringe oscillations on one qubit coupled to metamaterial ring resonator with and without an X pulse on second qubit.

Interfacial Optical Sensing of Ferroelectricity in Freestanding Perovskite Oxide by Using Monolayer Transition Metal Dichalcogenides

CNF Project Number: 2126-12
Principal Investigator(s): Gregory David Fuchs
User(s): Jaehong Choi

Affiliation(s): Applied and Engineering Physics, Cornell University

Primary Source(s) of Research Funding: Multidisciplinary University Research Initiatives (MURI) program

Contact: gdf9@cornell.edu, jc3452@cornell.edu

Primary CNF Tools Used: SC4500 Odd-Hour Evaporator, YES Asher, Anatech Resist Strip, GCA 6300 DSW 5X g-line Wafer Stepper, Heidelberg Mask Writer - DWL2000, Dicing Saw - DISCO, Wire Bonder

Abstract:

Two-dimensional (2D) transition metal dichalcogenides (TMDs) can be easily integrated with other functional materials such as ferroelectric materials due to their lack of dangling bonds. Also, owing to their atomic thickness, electronic and photoluminescence (PL) properties of 2D TMDs can be modulated by external perturbations, which opens new avenues for quantum sensing and optoelectronic devices. In this work, monolayer WSe_2 is integrated with a freestanding perovskite oxide $BaTiO_3$ (BTO) membrane. We observe that the relative density of charge carriers in WSe_2 changes as the polarization switches, and this gives rise to the PL intensity modulation. The relative emission intensity of neutral excitons (X^0) and trions (X^T) shows gate dependent hysteresis, which confirms that WSe_2 senses and optically reads out the ferroelectricity in BTO.

Summary of Research:

Perovskite oxides BTO have strong spontaneous polarization and moderate coercive field [1], but their epitaxial mother substrates often limit the range of device structures. Recent studies showed that perovskite oxides can be released from the substrate by using a sacrificial oxide layer [2-7], which allows integration with Si-based substrates. In our work, BTO is epitaxially grown on a $Sr_3Al_2O_6$ sacrificial layer and released in water. Isolated BTO is transferred onto a SiO_2/Si substrate (BTO growth and transfer done by Kevin Crust from the Hwang group at Stanford).

After this transfer, small BTO membranes with suitable size for device fabrication are picked up by using a polymer stamping method. Then, this freestanding BTO membrane is interfaced with WSe_2 to form a field effect device. In this device, the polarization in BTO can be switched *in-situ* by applying a gate voltage, and the polarization-induced PL modulation in monolayer WSe_2 is studied.

To study the ferroelectricity induced optical properties change in monolayer WSe_2, two voltage application modes are used: DC mode and pulse mode. In the DC mode, a continuous DC voltage is applied, and in the pulse mode, a DC mode voltage is applied for five seconds and then removed before taking spectra. In the DC mode, a negative voltage is applied to switch the polarization to an out-of-plane direction. When the polarization in BTO is in an out-of-plane direction, holes are induced in BTO near WSe_2/BTO.

In response to this polarization induced charges, the electron population increases in WSe_2, which facilitates X^0 formation in p-type WSe_2. As in Figure 1, X^0 emission intensity is enhanced when -6V was applied. When a positive voltage is applied, the polarization in BTO is flipped to an opposite direction, and electrons in BTO are accumulated near WSe_2/BTO. This results in hole accumulation in WSe_2 and leads to positively charged trion (X^+) emission intensity enhancement (Figure 1). When the voltage sweep direction is reversed, the PL modulation shows different behavior as in Figure 2. This asymmetry is the manifestation of the ferroelectricity of BTO. To further corroborate this, X^0 and X^+ emission peaks were resolved by using the Gaussian fitting method and their relative emission intensity (X^0/X^+) is plotted as a function of the gate voltage (Figure 3). X^0/X^+ shows a hysteresis loop, which confirms that the PL modulation in WSe_2 is induced by the polarization switching in BTO.

In the pulse mode, the hysteresis direction is changed (Figure 4). This is possibly due to the polarization decay after the voltage removal. Further study is needed to understand the mechanism of this hysteresis direction reversal in the pulse mode.

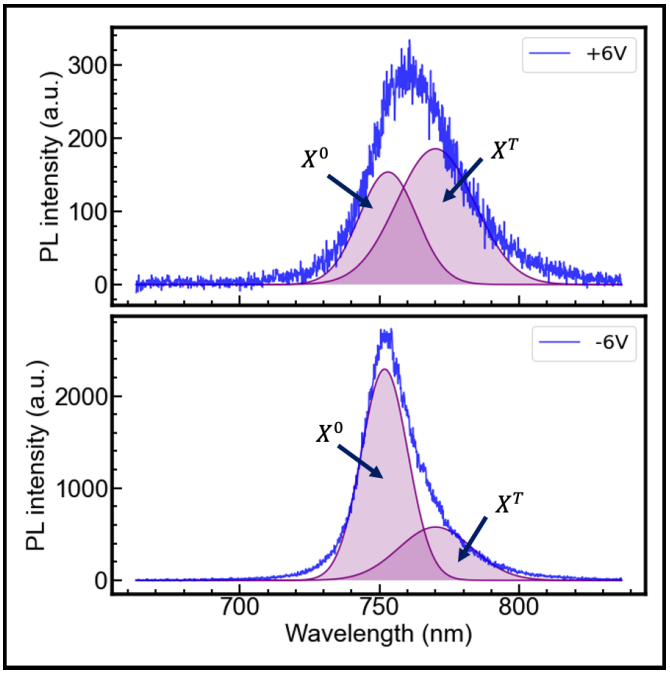

Figure 1: PL spectra at different gate voltage. X^0 and X^T emission is resolved by using the Gaussian fitting method. Spectrum at +6V (top) and spectrum at -6V (bottom).

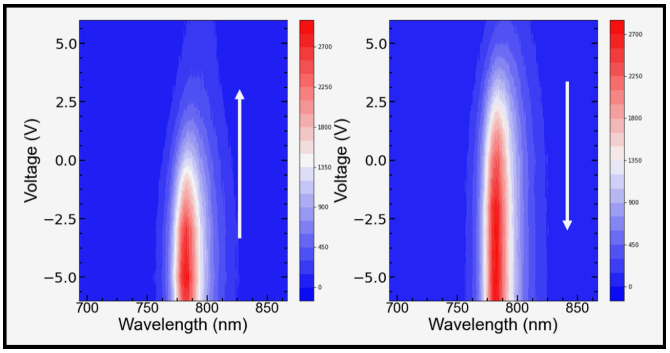

Figure 2: PL intensity modulation as a function of a gate voltage. PL intensity modulation shows different behavior when the voltage sweep direction is reversed.

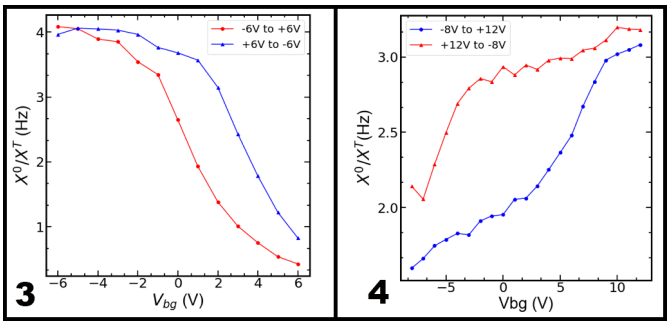

Figure 3, left: Relative ratio of X^0 and X^T emission (X^0/X^T) is plotted as a function of the DC gate voltage.

Figure 4, right: Relative ratio of X^0 and X^T emission (X^0/X^T) is plotted as a function of the pulsed gate voltage.

Conclusions and Future Steps:

In this work, we fabricate a freestanding BTO and monolayer WSe_2 based field effect device. The relative emission intensity of X^0 and X^T changes with the gate voltage and shows the hysteresis loop, which confirms that WSe_2 senses and optically reads out the polarization switching in BTO. As a next step, we will study the thickness dependent ferroelectricity in BTO by interfacing WSe_2 with BTO of various thickness. Also, BTO is known to have various phases at different temperatures [8]. We will explore the phase transitions in BTO by varying the temperature and study the optical and electronic property change in WSe_2 in response to the phase transition of BTO.

References:

[1] W. Gao,. et al. JOM 6 (2020).
[2] Lu, D., et al. Nature Mater 15, 1255-1260 (2016).
[3] Ji, D., et al. Nature 570, 87-90 (2019).
[4] Eom, K., et al. Science Advances 7 (2021).
[5] Bakaul, S., et al. Adv. Mater. 32, 1907036 (2020).
[6] Salles P., et al. Adv. Mater. Interfaces, 8, 2001643 (2021).
[7] Bakaul S. AIP Advances 11, 115310 (2021).
[8] Shu, Y.C., et al, Philos. Mag.B 81, 2021-2054 (2001).

Mechanically Driven Electron Spins with a Diamond Thin-Film Bulk Acoustic Resonator

CNF Project Number: 2126-12
Principal Investigator(s): Gregory David Fuchs[1]
User(s): Johnathan Kuan[2], Anthony D'Addario[2]
Collaborator(s): Sunil Bhave[3], Ozan Erturk[3]

Affiliation(s): 1. Department of Applied and Engineering Physics, Cornell University; 2. Department of Physics, Cornell University; 3. Department of Electrical and Computer Engineering, Purdue University

Primary Source(s) of Research Funding: Defense Advanced Research Projects Agency- DARPA DRINQS program (Cooperative Agreement #D18AC00024), Q-NEXT (U.S. Department of Energy, Office of Science, National Quantum Information Science Research Centers)

Contact: gdf9@cornell.edu, jk2788@cornell.edu, ajd344@cornell.edu

Website(s): https://fuchs.research.engineering.cornell.edu/

Primary CNF Tools Used: OEM Endeavor M1, Westbond 7400A Ultrasonic Wire Bonder

Abstract:

Lattice strain is an effective method of coherently manipulating electron spins in solid state defect centers such as the diamond nitrogen-vacancy center. To improve the achievable strain and power efficiency of bulk acoustic resonators for quantum control, we develop and characterize a released diamond thin-film bulk acoustic resonator. We demonstrate coherent driving of a double quantum transition of the NV electron spin through acoustically driven Rabi oscillations, achieving a Rabi frequency of 6 MHz. We also study the performance of the device over various powers and find that driving larger than 25 dBm deteriorates the performance of the FBAR.

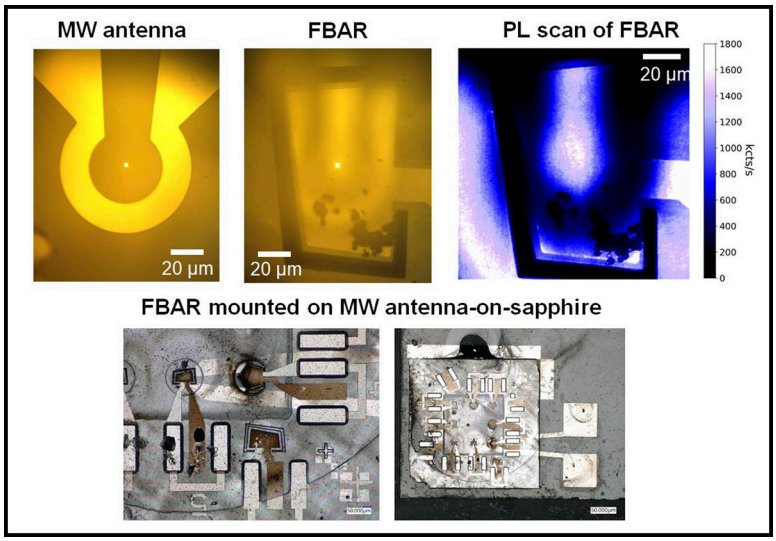

Figure 1: Microscope images of the MW antenna and FBAR device structure during our measurements, as well as a photoluminescence image of an AlN FBAR on diamond. The other two images are pictures taken of the FBAR device and antenna chip aligned on top of each other.

Summary of Research:

The diamond nitrogen-vacancy (NV) center is a solid-state defect consisting of a substitutional nitrogen adjacent to a lattice vacancy. The NV center electron spin interacts with many external fields (magnetic, electric, etc.), making it an excellent platform for quantum control and sensing. Acoustic control of the NV center with strain has been achieved with High Overtone Bulk Acoustic Resonators (HBARs) fabricated on diamond. The lattice strain provided by these devices have been used in experiments demonstrating coherent control and continuous dynamical decoupling for protecting electron spin coherence. In addition, strong driving on the electron spin can be used to protect the spin coherence of the native nitrogen spin of the NV center.

Strong driving of the electron spin can temporally average away the hyperfine interaction between the electron and nitrogen spin, effectively decoupling them. This opens avenues for using the nitrogen spin as a sensor, leveraging its long spin coherence time, while using the electron spin for optical initialization and readout.

To achieve strong driving of the electron spin with lattice strain, we fabricated a new generation of thin-film bulk acoustic resonators (FBAR) on single crystal diamond (Figure 1). The FBAR resonators consist of a 1.5 μm AlN transducer, with a bottom electrode and a top Pt electrode. The transducer deposited onto of a 10 μm thin optical grade diamond, which is created through reactive ion etching. The AlN film is sputtered using the OEM

Endeavor M1 tool at CNF. After fabricating the AlN transducer, we release the FBAR from the surrounding diamond via a backside etch. An antenna for magnetic control of the NV centers is fabricated on a separate sapphire chip that is bonded to the diamond before testing.

We perform measurements of this FBAR with an electromechanical mode at 1.9237 GHz. An external magnetic field is applied to tune the electron double quantum transition (ms = -1 to ms = +1) to be resonant with the mode. We coherently drive Rabi oscillations of to measure the strain generated by our device (Figure 2). As we increase the drive power, the oscillation frequency increases linearly. This continues up to a certain point, after which, the electromechanical response of the device is permanently degraded. The exact physical mechanism that is causing the degradation in performance is unclear, but we suspect that thermal heating due to the high power applied to the device plays a strong role, damaging the piezoelectric film and/or the Pt electrodes.

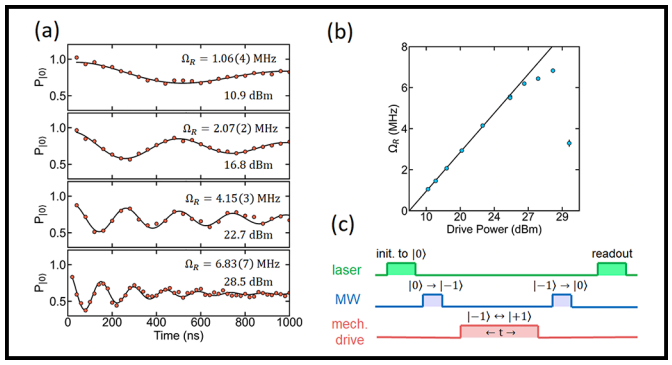

Figure 2: (a) Mechanical Rabi measurements as a function of applied power to the FBAR device. As we increase the power, the Rabi frequency increases. (b) Summary of all the mechanical rabi frequencies as a function of applied power. There is a linear relationship, until the electromechanical response of the device permanently changed with too much applied power. (c) Pulse sequence of the mechanical Rabi sequence used.

Conclusions and Future Steps:

We have developed a process for fabricating released AlN FBAR devices on diamond for NV sensing protocols. The next step is to investigate the cause of the degradation of the device performance at high powers. In addition, we hope to improve the process of depositing AlN on diamond, to mitigate losses introduced during sputtering and to consistently get high quality films.

Room Temperature Optically Detected Magnetic Resonance of Single Spins in GaN

CNF Project Number: 2126-12
Principal Investigator(s): Gregory David Fuchs[1], Farhan Rana[2]
User(s): Jialun Luo[3], Yifei Geng[2]

Affiliation(s): 1. School of Applied and Engineering Physics,
2. Department of Electrical and Computer Engineering; 3. Department of Physics; Cornell University

Primary Source(s) of Research Funding: Cornell Center for Materials Research (CCMR),
an NSF Materials Research Science and Engineering Center (DMR-1719875);
The NSF TAQS program (ECCS-1839196); Cornell Engineering Sprout program

Contact: gdf9@cornell.edu farhan.rana@cornell.edu, jl3562@cornell.edu yg474@cornell.edu

Website(s): http://fuchs.research.engineering.cornell.edu

Primary CNF Tools Used: AJA sputtering system, GCA 5x stepper

Abstract:

Optically detected magnetic resonance (ODMR) is an efficient mechanism to readout the spin of solid-state color centers based on spin-dependent relaxation between the optically excited states to the ground states. The detection of high contrast room temperature ODMR becomes the hallmark for a color center to become useful quantum sensors. Our work discovers such optically addressable spins in single defects hosted GaN. We measure two distinct ODMR responses from the defects with contrast as large as 30%, marking the existence of least two defect species in GaN. Our results lay the foundation for a promising quantum sensing platform and provide additional insights into the nature of GaN defects.

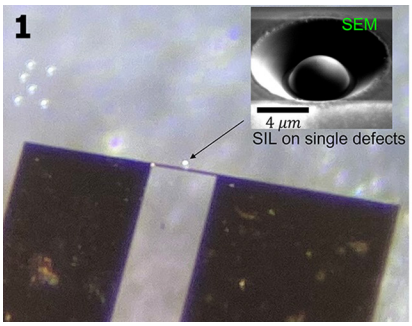

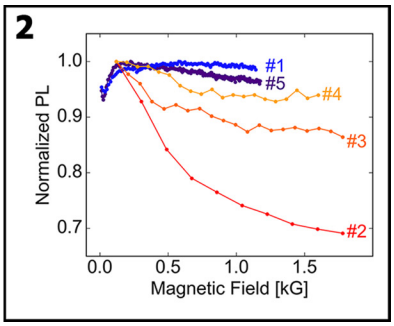

Figure 1, left: Microwave antennae under optical microscope. Inset: SEM of a solid-immersion lens. Figure 2, right: The magnetic field dependent PL of five defects.

Summary of Research:

Background. Room temperature ODMR has been detected in many solid-state color centers such as nitrogen-vacancy (NV) centers in diamond [1], silicon vacancy centers [2] and divacancy centers [3] in SiC, and recently in boron vacancy center ensembles [4,5] and unidentified single defects [6] in hexagonal boron nitride (hBN).

As the third-generation semiconductor, GaN is a mature platform with well-developed electronics applications owing to its wide direct bandgap and high breakdown field [7]. Recently, it has also been found to host bright single photon emitters with spectrally narrow photoluminescence (PL) in the visible spectrum [8,9]. These excellent optical properties, combined with the engineerability of GaN make these single-photon emitting defects attractive for on-chip photonics and relevant quantum technologies. However, the atomic structure of these defects has not yet been identified. We report [10] the discovery of high-contrast optically detected spin resonance, which is both interesting for identifying the defect structure, and for a potential application in quantum magnetometry.

Methods. We use a homebuilt laser scanning confocal microscope to measure the photoluminescence. To enhance the PL collection from the sample, we carve out a hemispherical solid-immersion-lens on top of the defect of interest with focused ion beam milling as seen in Figure 1a. We then use GCA 5x stepper to define the microwave antennae pattern and use the AJA sputter system to deposit a stack of Cr(10nm)/Cu(1um) to make the antennae shown in Figure 1b, which creates microwave that excites the spin resonances.

Results. Figure 2 shows the magnetic field dependent PL (magneto-PL) responses of 5 individual single defects, where the magnetic field is roughly aligned to the GaN crystal c-axis. Defects #1 and #5 show low PL at low magnetic field and saturate at high PL at high field. In

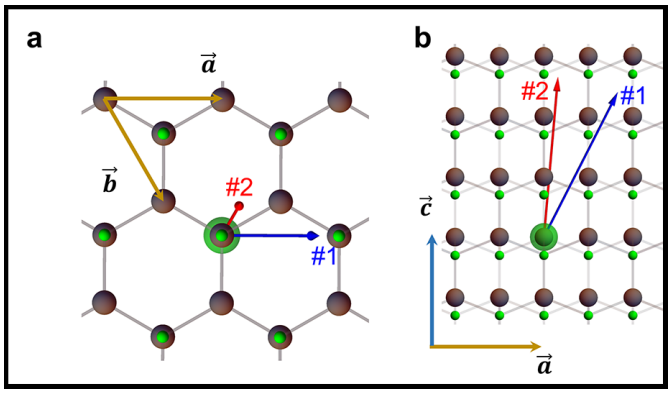

Figure 3: Spin quantization axes of defects #1 and #2 in a GaN lattice.

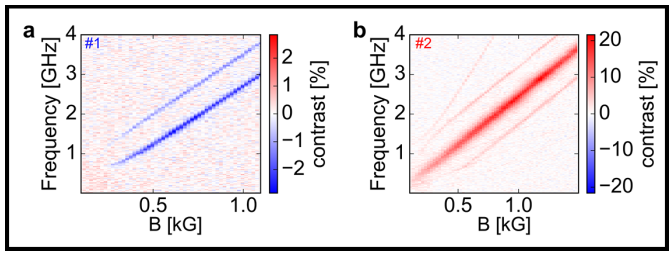

Figure 4: The ODMR spectra as a function of magnetic field of representative defects: defect #1 for group-I and defect #2 for group-II.

contrast, defects #2-#4 show monotonically decreasing PL as the magnetic field increases. The magneto-PL gives the first evidence of two distinct defect species with $S \geq 1$ spin.

The spin quantization axis is an important parameter for studying and revealing the nature of a new defect in solids. We examine the minimum Hamiltonian of a spin with $S \geq 1$ interacting with magnetic field $\vec{B}$ given by

$$H = DS_z^2 + E\left(S_x^2 - S_y^2\right) + g\mu_B \vec{S} \cdot \vec{B},$$

where S is the electronic spin operator, g the electronic g-factor, μ_B the Bohr magneton, D and E together the zero-field interaction parameters. An angle between the magnetic field $\vec{B}$ and the spin quantization axis introduces off-diagonal matrix elements between the spin eigenstates, mixing them and reducing the ODMR contrast. Thus, we find the spin quantization axes by measuring the angle resolved ODMR and finding the optimal angles that produce the largest contrast.

Figure 3 shows the spin quantization axes for defects #1 and #2, both of which lie in the a-plane but do not connect an atom with its n-th nearest neighbor for small n.

We can now further probe the spin Hamiltonian by measuring the magnetic field dependent ODMR, where the field is aligned with the spin axes. Figure 4 shows ODMR spectra of defects #1 and #2 as a function of magnetic field.

Defect #1 exhibits two negative contrast spin resonances that disperse with a gyromagnetic ratio of $\gamma_e = 2.8$ MHz/G, which confirms electron spins. The signal vanishes at low magnetic field because the spin sublevels become degenerate and mix with each other. The data can be fit by $D \approx E \approx 400$ MHz for a spin-1 Hamiltonian.

Defect #2 shows a total of four positive contrast resonances, where three of them disperse with γ_e and one with $2\gamma_e$. Worth noted is that the maximum contrast of the spin resonance of defect #2 is as large as 30%. The number resonances require a minimum model of spin-3/2 system. However, the minimum Hamiltonian can only account correctly for the three resonances that disperse with γ_e when $D \approx 370$ MHz and $E = 0$, pointing to additional terms required in the Hamiltonian.

The ODMR signatures corroborate that there are at least two different species of optically addressable single spin defects in GaN.

Acknowledgements:

We thank Len van Deurzen, Debdeep Jena, and Huili Grace Xing for useful discussions and for supplying the GaN substrates. We thank Brendan McCullian, Nikhil Mathur, Anthony D'Addario, and Johnathon Kuan for very helpful discussions on physics and microwave experiments.

References:

[1] Doherty, M. W., et al. Physics Reports 528, 1-45 (2013).
[2] Widmann, M., et al. Nature Mater 14, 164-168 (2015).
[3] Koehl, W. F., Buckley, B. B., Heremans, F. J., Calusine, G., and Awschalom, D. D. Nature 479, 84-87 (2011).
[4] Gottscholl, A., et al. Nat. Mater. 19, 540-545 (2020).
[5] Gao, X., et al. Nano Lett. 21, 7708-7714 (2021).
[6] Chejanovsky, N., et al. Nat. Mater. 20, 1079-1084 (2021).
[7] Milligan, J. W., et al. 2007 IEEE Radar Conf. 960-964 (2007).
[8] Geng, Y., et al. Sci Rep 13, 8678 (2023).
[9] Geng, Y., Jena, D., Fuchs, G. D., Zipfel, W. R., and Rana, F. Preprint at arXiv:2306.17339 (2023).
[10] Luo, J., Geng, Y., Rana, F., and Fuchs, G. D. Preprint at arxiv:2306.12337 (2023).

Coherent Acoustic Orbital Control of Diamond NV Center Excited States

CNF Project Number: 2126-12
Principal Investigator(s): Gregory David Fuchs
User(s): Brendan Andrew McCullian

Affiliation(s): School of Applied and Engineering Physics, Cornell University

Primary Source(s) of Research Funding: DARPA Driven and Nonequilibrium Quantum Systems (DRINQS) Program, Department of Energy Office of Basic Energy Sciences, Office of Naval Research

Contact: gdf9@cornell.edu, bam327@cornell.edu

Primary CNF Tools Used: GCA 6300 DSW 5X g-line Wafer Stepper, Heidelberg Mask Writer - DWL2000, AJA Sputter Deposition, Westbond 7400A Ultrasonic Wire Bonder

Abstract:

The spectrally narrow, spin-dependent optical transitions of nitrogen-vacancy (NV center) defects in diamond have been shown to be a promising platform for quantum networking. The entanglement generation rates of such networks suffer from spectral diffusion that originates from electric field fluctuations in the diamond, which couple to the excited state orbital doublet and alter the optical frequencies. With the motivation of better understanding how orbital decoherence can be overcome, we investigate quantum control of the excited state orbitals using gigahertz frequency strain. We show that coherent, multi-phonon orbital Rabi oscillations can be acoustically driven on nanosecond timescales. Additionally, we investigate orbital Rabi splitting in spectroscopy, finding good agreement between the measured orbital Rabi rate found by the two detection methods.

Summary of Research:

Diamond NV centers are a promising platform for quantum networking applications owing to their spectrally narrow, spin-preserving optical transitions at cryogenic temperatures [1]. Spectral diffusion of the optical transition frequencies decreases the entanglement generation rate [2,3]. Spectral diffusion originates from fluctuations of the local electric field environment of the defects and the coupling of these electric field fluctuations to the excited state orbital doublet which alters the optical transition frequencies and diminishes coherence [4].

Our recently published work studying the correlations between spectral diffusion and other physical parameters of the NV center found correlation with static strain [5]. Related to this, we have previously studied the coupling of GHz frequency acoustic waves to the excited state orbitals [6]. These results indicate that for some NV centers the optical transitions may be stabilized by coherently driving the excited state orbital transition using acoustic waves. With this idea in mind, we set out to demonstrate coherent acoustic orbital control in the time domain.

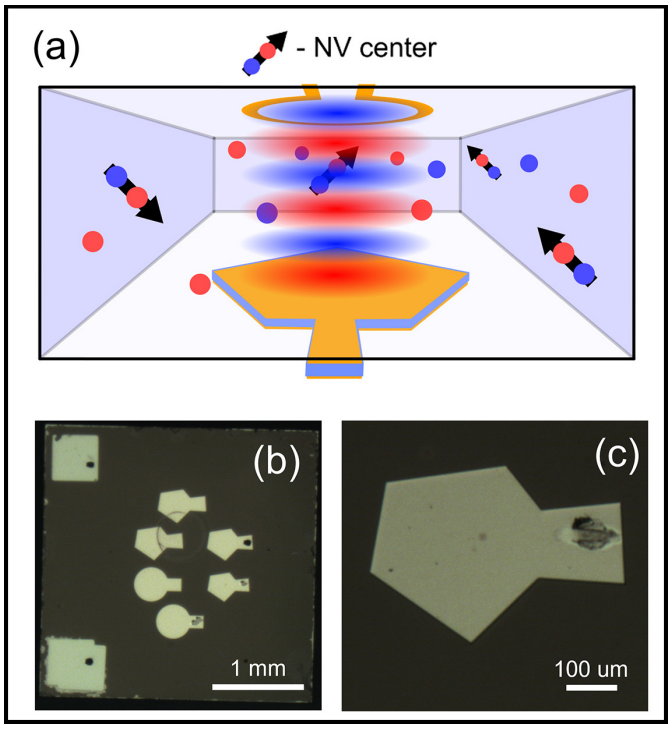

Figure 1: (a) Schematic of HBAR-on-diamond device for acoustic orbital control. HBAR transducer (orange pentagon) on diamond surface launches GHz frequency strain waves (red and blue ovals) into diamond bulk where the dynamic strain interacts with bulk NV centers. (b,c) Optical micrograph of finished HBAR-on-diamond device showing several finished HBARs on the diamond chip.

Our sample (Figure 1) is a type IIa diamond with individually addressable single NV centers formed via electron irradiation and subsequent annealing. On one diamond surface we fabricated a high-overtone bulk acoustic-wave resonator (HBAR) capable of launching GHz-frequency strain waves into the diamond bulk.

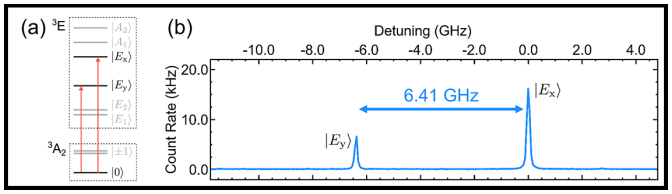

Figure 2: (a) Spin-preserving optical transitions of the spin-0 subspace (red arrows) of the NV center. (b) Laser-frequency swept PLE spectroscopy of a single NV center showing 6.41 GHz orbital splitting.

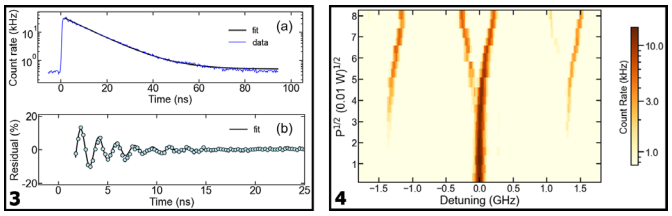

Figure 3, left: (a) Time-resolved histogram of photons emitted from our defect with respect to 1 ns resonant laser pulses (blue curve) while the HBAR is mechanically driven at 1.29 GHz. Exponential fit (black curve) used to remove exponential decay and extract residual oscillation. (b) Residual oscillation showing ns-scale precession of the orbital states in the strain field. Black fit is to a decaying sinusoid. Figure 4, right: (a) Frequency-swept PLE near the Ex transition versus acoustic drive power showing orbital splitting with increasing acoustic drive power.

The HBAR is formed by sandwiching a piezoelectric layer in between metal electrodes. The bottom electrode layer ([Ti (15 nm)/Pt (90 nm)] was deposited using the AJA Sputter Deposition system. A 1.2 μm thick layer of piezoelectric zinc oxide was then sputtered using equipment the Cornell Center for Materials Research. Finally, the top metal electrodes ([Ti (15 nm)/Pt (180 nm)] were fabricated by using the Heidelberg Mask Writer - DWL2000 to make the mask, the GCA 6300 DSW 5X g-line Stepper to write the pattern, and the AJA Sputter Deposition system to deposit the metals. After lift-off the device was wire bonded to our cryostat microwave feed lines using the Westbond 7400A Ultrasonic Wire Bonder.

We characterize the static strain splitting of a single bulk NV center in the diamond by performing photoluminescence excitation (PLE) spectroscopy [7]. We tune a red laser (~637.2 nm) across the resonant optical transitions of the NV center while counting photons emitted into the phonon sideband. The spin-preserving optical transitions are from orbital singlet, spin triplet ground states to orbital doublet, spin triplet excited states [4]. All measurements are carried out in a helium flow cryostat at 7 K. We focus solely on the spin-0 subspace. PLE spectroscopy of our defect reveals a 6.41 GHz splitting between the spin-0 orbital excited states which results from static strain in the diamond (Figure 2).

We perform time-domain resonant orbital driving experiments by tuning a red laser (~637.2 nm) onto resonance with an optical transition between the spin-0 ground state and one of the spin-0 orbital transitions (Figure 3). While continuously driving our acoustic resonator at 1.29 GHz (such that we excite orbital transitions via a 5-phonon drive) we provide 1 ns resonant laser pulses and record the arrival time of emitted photons relative to the excitation laser pulses. We observe an expected exponential decay of photoluminescence resulting from spontaneous emission as the defect leaves the excited state, and a residual photoluminescence oscillation which results from coherent orbital oscillations driven by the HBAR.

We confirm that these time domain oscillations are the result of the acoustic driving by performing PLE spectroscopy in the presence of acoustic drive (Figure 4). We observe a splitting of the PLE spectrum as the acoustic driving amplitude increases which results from coherent orbital driving. The splitting of the PLE spectrum from acoustic drive matches well with the frequency of the time-domain orbital oscillations, confirming that they originate from the same physics.

Conclusions and Future Steps:

Our results indicate that the excited state orbital doublet of NV centers can be coherently driven via acoustic drive. We confirm that our observed oscillations in the time domain match with the splitting observed in resonant optical spectroscopy under acoustic drive. Coherent orbital control will enable future studies of orbital and optical coherence of NV centers [8] under acoustic drive, where we can quantify the orbital and optical coherences and investigate orbital dynamic decoupling.

Our manuscript on time-domain coherent acoustic orbital control is currently under preparation.

References:

[1] L. Childress, et al., Phys. Rev. A 72, 052330 (2005).
[2] K. M. C. Fu, et al., Phys. Rev. Lett. 103, 256404 (2009).
[3] S. L. N. Hermans, et al., Nature 605, 663 (2022).
[4] J. R. Maze, et al., New J. Phys. 13, 025025 (2011).
[5] B. A. McCullian, et al., Phys. Rev. Appl. 18, 064011 (2022).
[6] H. Y. Chen, et al., Phys. Rev. Lett. 120, 167401 (2018).
[7] K. W. Lee, et al., Phys. Rev. Appl. 6, 034005 (2011).
[8] L. C. Bassett, et al., Science 345, 6202 (2014).

Nanostructure Integrated Silicon Vacancy in 4H-Silicon Carbide

CNF Project Number: 2126-12
Principal Investigator(s): Gregory David Fuchs
User(s): Jae-Pil So

Affiliation(s): Applied and Engineering Physics, Cornell University

Primary Source(s) of Research Funding: National Science Foundation, OMA.2137828

Contact: gdf9@cornell.edu, js3338@cornell.edu

Primary CNF Tools Used: Oxford COBRA, Oxford 81 Etcher, 5X g-line stepper, Dicing saw - DISCO, SC4500 Odd hour Evaporator, AJA Sputter, Zeiss Supra SEM, Zeiss Ultra SEM, Nabity

Abstract:

Silicon vacancy (V_{si}) centers in 4H-silicon carbide (4H-SiC) has emerged as a candidate for quantum networking applications owing to its outstanding physical properties including a long spin coherence time, a high Debye-Waller factor, and its status in a mature semiconductor with established fabrication recipes. However, the out-of-plane orientation of optical dipole of VSi introduces a challenge for optically exciting it with a free-space laser, and coupling it external optical structures. Here we demonstrate fabrication of SiC nanowires using metal-assisted chemical etching (MACE) that can be cleaved mechanically and transferred on the other substrates. Also, we demonstrate combining V_{si} with a plasmonic cavity that enhances the emission rate.

Summary of Research:

Optically accessible spin states in solids are a promising basis for establishing a quantum networking platform. 4H-SiC offers a unique opportunity for on-chip quantum photonics, as it hosts a variety of optically accessible defects [1,2]. V_{si} in 4H-SiC has shown excellent optical coherence at cryogenic temperatures with millisecond spin-coherence time, and coherent coupling to nuclear spins [3-5]. However, the out-of-plane orientation of its optical dipole prevents it from being excited by a free-space pump laser that produces only in-plane electric field oscillation. Here, we demonstrate the fabrication of SiC nanowires using a top-down method, allowing nanowires that can be cleaved mechanically and transferred on the other substrates [6]. This approach enables the excitation of the optical dipole, which is now elongated along the in-plane direction. Also, we demonstrate combining V_{si} with a plasmonic silver nanopan cavity which has both transverse electric (TE) and magnetic (TM) modes [7].

To demonstrate SiC nanowires with embedded V_{si}, we use a metal-assisted chemical etching (MACE) technique (Figure 1a) [6]. First, a monolayer polystyrene bead array is dispersed on entire SiC chip using DI-water batch

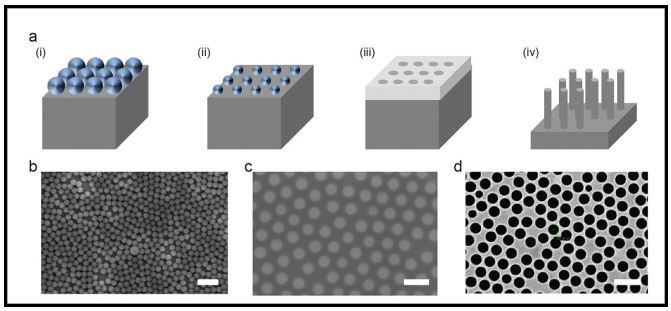

Figure 1: (a) Schematic of the fabrication procedures to create SiC nanowire. (b,c) SEM images of the polystyrene beads array on SiC substrate (b) before and (c) after reducing the diameter via RIE. Scale bar, 3 mm and 500 nm, respectively. (d) SEM image of the Pt mesh. Scale bar, 500 nm.

(Figure 1b). Next, the diameter of the beads are reduced to 260 nm to free up space between the beads via reactive ion etching (RIE) as shown in Figure 1c. Then we obtain Pt mesh via typical metal deposition method using e-beam evaporation (Figure 2d). The hole diameter of the Pt mesh determines the diameter of the SiC nanowire to be fabricated. Lastly, the SiC substrate with the PT mesh is immersed in etching solutions of $HF:H_2O_2:H_2O$ (volume ratio = 5:1:6) at room temperature while Pt mesh act as an etching catalyst. The etching front of the SiC substrate moves downward vertically, which results in the formation of vertical SiC nanowire arrays.

After being cleaved and transferred onto the Si/SiO_2 substrate, we perform optical measurements of the single nanowires using confocal laser microscope setup with continuous-wave 785 nm laser and two scanning mirrors at 10 K. The light emission from the nanowire is collected by objective lens and sent to avalanche photodiodes or monochromator/charge-coupled device via optical fibers. Figure 2a shows the measured photoluminescence (PL) intensity map of the SiC nanowire at 10 K. Bright emission spots are observed at the end of the nanowire probably due to scattered emission at the end facet of it. Additionally, the PL spectrum measured at the brightest spot exhibit three emission peaks at 859.1 nm, 861.6 nm,

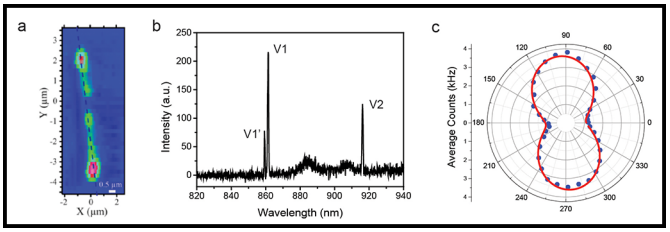

Figure 2: (a) Measured PL intensity map for the SiC nanowire on the Si/SiO_2 substrate. The pump power was 105 mW. Scale bar, 500 nm. (b) PL spectrum measured at the brightest spot in (a). (c) Polar plot of the emission as a function of the polarization angle. The line indicates the fitted curve.

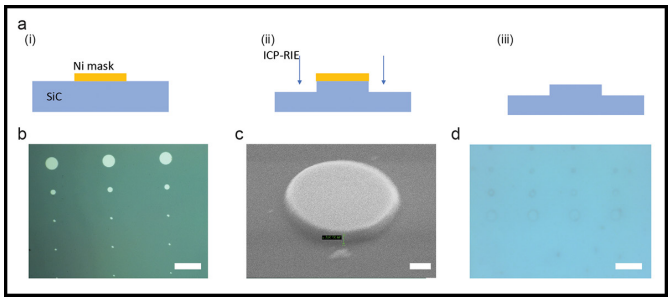

Figure 3: (a) Schematic of the fabrication procedures for SiC-Ag nanopan structure. (b) Optical microscope image of Ni masks on SiC substrate. Scale bar, 20 mm. (c) SEM image of the SiC disk prior to silver encapsulation. Scale bar, 500 nm. (d) Optical microscope image of the SiC-Ag nanopan structure from the back side of the wafer. Scale bar, 20 mm.

and 914.1 nm, which corresponds to the V1', V1, and V2 emission, respectively. This means that elongation of optical dipole along the in-plane direction enables observation of all emission lines under free-space laser pumping. To verify the optical dipole orientation of the emission, we performed emission polarization measurements. Figure 2c shows the emission polarization data obtained from the same spot used in Figure 2b and the corresponding fitting curve obtained using a cos2(q) fitting function. The emission polarization visibility is calculated to be 76% elongated along axial direction of the nanowire as expected.

Next, to demonstrate a plasmonic cavity coupled V_{si} in 4H-SiC, we employ silver nanopan resonator encapsulating the SiC microdisk structure. Figure 3a shows the fabrication procedure. First, a circular shape Ni mask with a thickness of 100 nm is deposited on 4H-SiC wafer which contains V_{si} using e-beam lithography and metal evaporation technique (Figure 3b). Next, inductively coupled plasma-reactive ion etching (ICP-RIE) is performed to etch the SiC layer (Figure 3c), and subsequently the Ni mask is removed using a Ni etchant (Figure 3d). After removing the Ni mask, 400.nm-thick silver layer is coated on the whole surface of the SiC disk substrate using an e-beam evaporator.

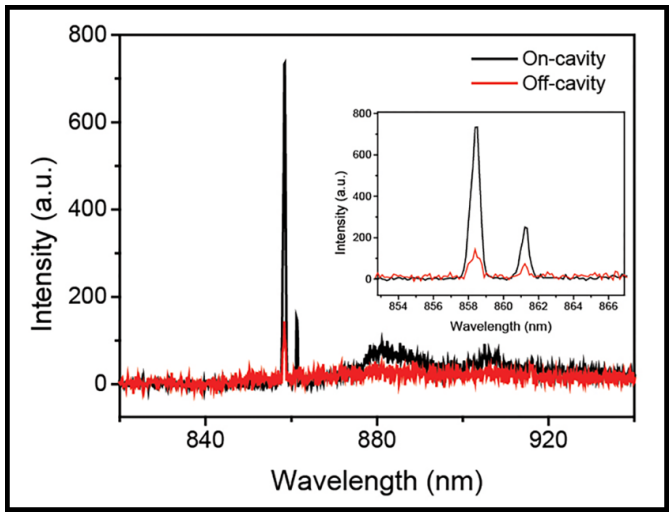

Figure 4: PL spectra measured at the nanopan (black) and the flat substrate (red). Inset shows the close-up of the emission peaks.

To access initially the characteristics of the nanopan combined V_{si}, we optically pump the nanopan region using a 785 nm continuous-wave laser and compare the emission spectrum to that from the flat surface at 10 K. We observe a 4-fold enhancement of V1' emission and 5-folds enhancement of V1 emission at the same time (Figure 4). The V1' emission is polarized along in-plane direction is predicted to couple to the TE whispery gallery mode (WGM), whereas V1 emission is probably coupled to the TM WGM.

Conclusions and Future Steps:

In this work, we demonstrate the integration of V_{si} in 4H-SiC with two types of nanostructures that enable us to excite the V1 emission via free-space laser pumping. In the future, we plan to perform the time-resolved PL measurements to extract the Purcell factor of this cavity-coupled emitter system. Also, it might be possible to apply microwave excitation to the emitter to mix the ground spin states, which will enable us to observe photoluminescence excitation (PLE) under resonant excitation.

References:

[1] Lukin, D., et al., Nat. Photonics 14, 330-334 (2020).
[2] Crook, A., et al., Nano Lett. 20, 3427-3434 (2020).
[3] Nagy, R., et al., Nat. Commun. 10, 1954 (2019).
[4] Widmann, M., et al., Nat. Mater. 14, 164-168 (2015).
[5] Babin, C., et al., Nat. Mater. 21, 67-73 (2022).
[6] Kim, J., et al., Nat. Nanotechnol. 12, 963-968 (2017).
[7] Kwon, S., et al., Nano Lett. 10, 3679-3683 (2010).

Exciton Density Waves in Coulomb-Coupled Dual Moiré Lattices

CNF Project Number: 2633-18
Principal Investigator(s): Jie Shan, Kin Fai Mak
User(s): Yihang Zeng, Zhengchao Xia

Affiliation(s): Laboratory of Atomic and Solid State Physics, Applied and Engineering Physics; Cornell University

Primary Source(s) of Research Funding: NSF, DOE, ONR

Contact: jie.shan@cornell.edu, kinfai.mak@cornell.edu, yz425@cornell.edu, zx287@cornell.edu

Primary CNF Tools Used: Autostep i-line Stepper, Hamatech Wafer Processor Develop, Heidelberg Mask Writer - DWL2000, Photolithography Spinners, SC4500 Odd/Even-Hour Evaporator, Dicing Saw - DISCO, Zeiss Supra SEM, Nabity Nanometer Pattern Generator System (NPGS)

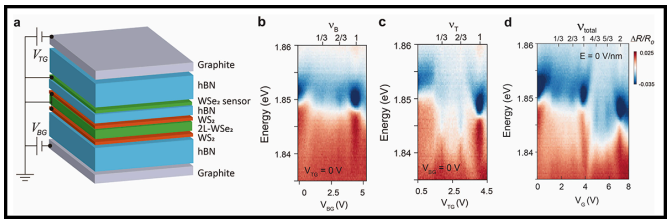

Figure 1: a, Schematic of a dual-gated device. b-d, Reflectance contrast spectrum of the sensor 2s exciton as a function of gate voltage and filling factor. In b, c one of the lattices is empty and in d two lattices are equally populated.

Abstract:

Strongly correlated bosons in a lattice are a platform to realize rich bosonic states of matter and quantum phase transitions, but in a solid-state system they are challenging to realize [1]. Here we trap interlayer excitons (bosons composed of bound electron-hole pairs) in a lattice provided by an angle-aligned WS_2/bilayer WSe_2/WS_2 heterostructure. We observe correlated insulating states when the combined electron filling factor of the two lattices equals to 1/3, 2/3, 4/3, and 5/3. These new states can be interpreted as exciton density waves in a Bose-Fermi mixture. Our results demonstrate that Coulomb-coupled moiré lattices are fertile ground for correlated many-boson phenomena.

Summary of Research:

Two-dimensional moiré materials have emerged as a highly tunable platform for the study of strongly correlated phases of matter. However, compared to fermionic systems, strongly correlated bosonic systems are much less explored. Here, we demonstrate the realization of a Coulomb-coupled dual-moiré lattice where electrons in one lattice bind with holes in the other forming bosonic particles (excitons). In such a system, we achieve independent control of the electron and exciton densities. When the combined electron filling factor of the two lattices is tuned to 1/3, 2/3, 4/3, and 5/3, we observe a new exciton density wave phase where an exciton fluid breaks the translational symmetry.

Figure 1a illustrates a dual-gated device of an angle-aligned monolayer WS_2/bilayer WSe_2/monolayer WS_2 structure. The WSe_2 bilayer provides nearly identical triangular moiré lattices of period $a_M \approx 8$ nm at the top and bottom WS_2/WSe_2 interfaces [2] and also acts as a tunnel barrier. For the relevant density range, the electrostatically doped electrons are in the WS_2 layers. The two graphite gates independently control the combined filling factor ν (doping density per moiré lattice) and the out-of-plane electric field E in two moiré lattices. The latter tunes the distribution of electrons between the two lattices. To probe the insulating states in the coupled moiré lattices, we employ an optical sensing technique [3] by placing a WSe_2 monolayer above the top WS_2 layer. Figure 1b-d show the reflectance contrast (RC) spectrum of the sensor 2s exciton as a function of gate voltage (lower axis) and total filling factor (upper axis). An insulating state in the sample is identified when the 2s exciton resonance exhibits a blueshift and an enhanced spectral weight 11. When the electrons are in one of the lattices solely (Figure 1b, c), insulating states are observed at $\nu = 1/3, 2/3, 1, 2$. When the electrons are introduced equally in two lattices by setting $E \approx 0$ V/nm (Figure 1d), we observe additional insulating states at $\nu = 4/3, 5/3$.

We use the amplitude of the sensor 2s exciton RC, R_{2s}, to identify insulating states. The largest R_{2s} is observed in Figure 2a when both lattices have integer fillings (ν_t and ν_b denoting the filling factor of the top and bottom lattices, respectively). We also observe extended regions with enhanced R_{2s} when the top lattice is insulating, and the bottom generally charge-compressible. They correspond to the red regions in Figure 2c. Similarly, one can find the blue regions in the electrostatic phase diagram in Figure 2c when the bottom lattice is insulating, and the top is generally charge-compressible. The result is fully consistent with an independent measurement based on the moiré excitons in WS_2 (Figure 2b).

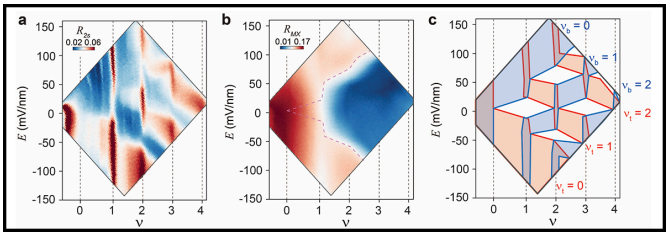

Figure 2: a,b, Reflectance contrast amplitude of the sensor 2s exciton R_{2s} (a) and WS_2 moiré exciton R_{MX} (b) as a function of total filling factor and electric field. c, Electrostatic phase diagram includes regions of gapped top lattice (red-shaded) and bottom lattice (blue-shaded).

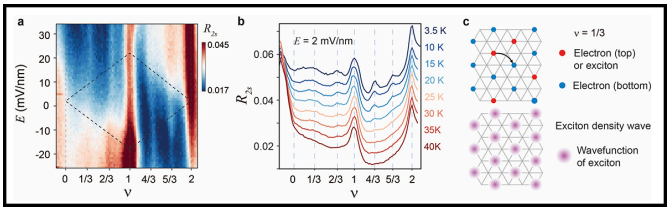

Figure 3: a, R_{2s} as a function of total filling factor and electric field. b, Horizontal linecut of a near zero field at representative temperatures. c, Schematic representation of the inter-layer Wigner crystal at ν=1/3.

Upon a closer examination, we identify incompressible states from the enhanced R_{2s} at $\nu = 1/3, 2/3, 1, 4/3, 5/3$ for a wide range of electric field (Figure 3a). As temperature increases, the incompressible states at the fractional fillings disappear around 30-35 K (Figure 3b). The nature of these insulating states inside the dashed box is completely different from outside the box. We focus on the exotic fractional fillings. They are generalized Wigner crystals when electrons reside in a single lattice (outside the box). Inside the box, electrons are continuously transferred from the generalized Wigner crystal to the empty lattice as a function of electric field but remain bound to the empty sites in the original lattice by the inter-lattice long-range Coulomb repulsion. They form an "inter-layer" Wigner crystal to minimize the total intra- and inter-lattice Coulomb repulsions and can also be viewed as excitonic insulators [4]. The interlayer excitons hop along the channels defined by the Wigner crystal (Figure 3c), therefore dubbed exciton density wave (EDW). In the weak-disorder limit, EDWs are expected to possess finite superfluid densities in the ground state and are supersolids, as predicted by theoretical studies on atomic Bose-Fermi mixtures. This is an interesting direction for future studies.

References:

[1] Ma, L., Nguyen, P.X., Wang, Z., Zeng, Y., Watanabe, K., Taniguchi, T., MacDonald, A.H., Mak, K.F., and Shan, J. Strongly correlated excitonic insulator in atomic double layers. Nature 598, 585-589 (2021).

[2] Tang, Y., Li, L., Li, T., Xu, Y., Liu, S., Barmak, K., Watanabe, K., Taniguchi, T., MacDonald, A.H., and Shan, J. Simulation of Hubbard model physics in WSe_2/WS_2 moiré superlattices. Nature 579, 353-358 (2020).

[3] Xu, Y., Liu, S., Rhodes, D.A., Watanabe, K., Taniguchi, T., Hone, J., Elser, V., Mak, K.F., and Shan, J. Correlated insulating states at fractional fillings of moiré superlattices. Nature 587, 214-218 (2020).

[4] Gu, J., Ma, L., Liu, S., Watanabe, K., Taniguchi, T., Hone, J.C., Shan, J., and Mak, K.F. Dipolar excitonic insulator in a moiré lattice. Nature Physics (2021).

Gate-Tunable Heavy Fermions in a Moiré Kondo Lattice

CNF Project Number: 2633-18
Principal Investigator(s): Jie Shan, Kin Fai Mak
User(s): Wenjin Zhao, Bowen Shen, Zhongdong Han, Kaifei Kang

Affiliation(s): Kavli Institute at Cornell for Nanoscale Science, Laboratory of Atomic and Solid State Physics, School of Applied and Engineering Physics; Cornell University

Primary Source(s) of Research Funding: DOE, NSF, AFOSR

Contact: jie.shan@cornell.edu, kinfai.mak@cornell.edu, wz435@cornell.edu, bs792@cornell.edu, zh352@cornell.edu, kk726@cornell.edu

Primary CNF Tools Used: Zeiss Supra SEM, Nabity Nanometer Pattern Generator System (NPGS), SC4500 Odd/Even-Hour Evaporator, Autostep i-line Stepper, Hamatech Wafer Processor Develop, Heidelberg Mask Writer - DWL2000, Photolithography Spinners, Dicing Saw - DISCO

Abstract:

The Kondo lattice—a matrix of local magnetic moments coupled through spin-exchange interactions to itinerant conduction electrons—is a prototype of strongly correlated quantum matter [1,2]. We realize a synthetic Kondo lattice in AB-stacked $MoTe_2/WSe_2$ moiré bilayers, in which the $MoTe_2$ layer is tuned to a Mott insulating state, supporting a triangular lattice of local moments, and the WSe_2 layer is doped with itinerant conduction carriers. We observe heavy fermions with a large Fermi surface below the Kondo temperature. We also observe the destruction of the heavy fermions with an abrupt decrease in the Fermi surface size and quasi-particle mass under an external magnetic field. We further demonstrate widely and continuously gate-tunable Kondo temperatures through the itinerant carrier density or the Kondo coupling.

Summary of Research:

Common approaches to realizing strong electronic correlations rely on intermetallic compounds that involve heavy elements like lanthanides [1,2]. The use of naturally occurring elements limits the found material's tuneability. Further, these materials typically have a very complex electronic structure, which makes them hard to describe and predict by theory. We demonstrate a model Kondo system created by stacking a pair of monolayer semiconductors to study quantum phenomena ranging from heavy fermions to exotic quantum phase transitions. We use $MoTe_2/WSe_2$ moiré bilayers, in which the $MoTe_2$ layer is tuned to a Mott insulating state, supporting a triangular moiré lattice of local moments, and the WSe_2 layer is doped with itinerant conduction carriers [3,4]. We observe heavy fermions with a large Fermi surface below the Kondo temperature T^* and that the heavy fermions be destructed by an external magnetic field. The Kondo temperature can be tuned widely and continuously via an applied electric voltage. The study opens the possibility of *in situ* access to the phase diagram of the Kondo lattice with exotic quantum criticalities in a single device based on semiconductor moiré materials [5].

Figure 1 shows the schematic and optical image of a device. We fabricated dual-gated $MoTe_2/WSe_2$ devices using a layer-by-layer dry-transfer technique. We deposited 5-nm Pt contacts on hBN by standard electron-beam lithography and evaporation, followed by another step of electron-beam lithography and metallization to form a bilayer of 5-nm Ti and 40-nm Au to connect the thin Pt contacts on hBN to pre-patterned electrodes.

Figure 2 shows the temperature dependence of the resistance R_{xx} when the device is tuned to a Kondo lattice phase. There is a characteristic temperature T^*, below which resistance drops significantly, and T^* increases with the hole density in the WSe2 layer (ν_W). The inset shows the T^2-dependence of R_{xx} at low temperatures, which is a characteristic of a Landau Fermi liquid. We fit the dependence using $R_{xx} = R_0 + AT^2$, where R_0 is the residual resistance, and $A^{1/2}$ is linearly proportional to the quasiparticle mass. The value is more than an order of magnitude larger than in the region without the formation of the Kondo lattice in the same device. The large enhancement points to the emergence of heavy fermions.

Figure 3 shows the magnetic-field dependence of the Hall density, $\nu^* = B/(eR_{xy}n_M)$ for $\nu_W = 0.35$. We obtain $\nu^* \approx -\nu_W$ for $\nu_{Mo} = 2$, where the Kondo lattice is not formed. For $\nu_{Mo} = 1$, below critical magnetic field (B_c) we obtain $\nu^* \approx 1-\nu_W$. It indicates a hole Fermi surface with density of $1 + \nu_W$.

This result shows that the local moments in the $MoTe_2$ layer are hybridized with the conduction holes in the WSe_2 layer to form a large hole Fermi surface. The observed large Fermi surface, in combination with the

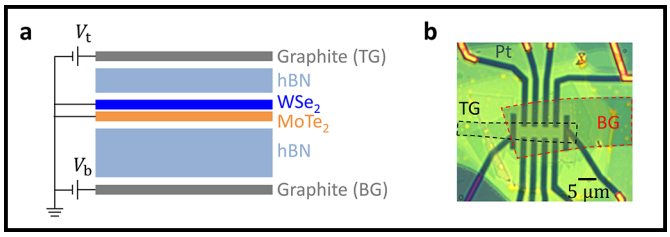

Figure 1: a, Device schematics. b, Optical microscope image of a dual-gated device. The scale bar is 5 μm.

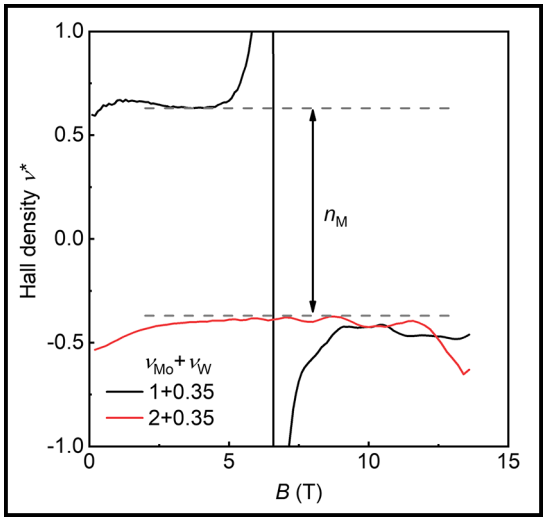

Figure 3: The corresponding magnetic-field dependence of the Hall density ν^* for $\nu = 1 + 0.35$ and $\nu = 2 + 0.35$. A density jump equaling the moiré density n_M occurs around 6 T.

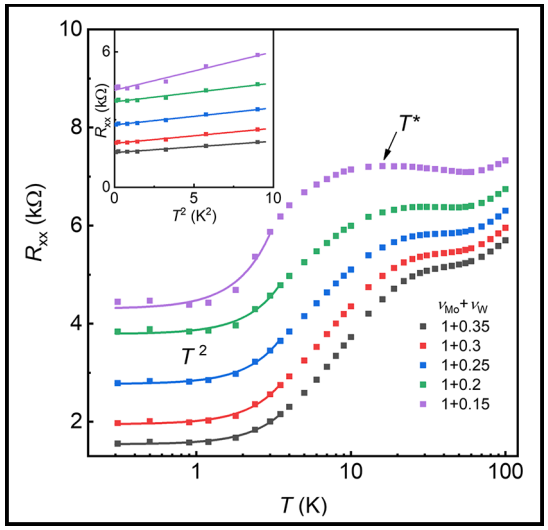

Figure 2: Temperature dependent longitudinal resistance R_{xx} at varying doping densities for $\nu = 1+ \nu_W$. The solid lines are the best fits to the quadratic temperature dependence at low temperatures. The arrows mark the Kondo temperature T^*. The insets show the scaling of R_{xx} with T^2.

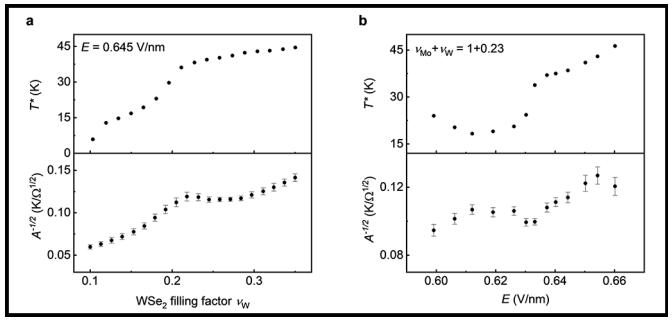

Figure 4: a, Extracted doping dependence of T^* (top) and $A^{-1/2}$ (bottom) at a fixed electric field (E=0.645 V/nm) for $\nu = 1 + \nu_W$. The two quantities show similar dependences. b, Extracted electric-field dependence of T^* (top) and $A^{-1/2}$ (bottom) at a fixed filling factor (ν=1+0.23).

quasiparticle mass enhancement, supports the realization of the Kondo lattice. The Hall measurement also shows that the large Fermi surface with hole density $1 + \nu_W$ is reduced to a small Fermi surface with hole density ν_W when a magnetic field above B_c is applied.

Figure 4 shows the tunability of the Kondo temperature T^* and the parameter $A^{-1/2}$. We show one cut along $E = 0.645$ V/nm (Figure 4a) and another cut along $\nu_W = 0.23$ (Figure 4b). The Kondo temperature (top panels) can be widely tuned by both doping and electric field. And $A^{-1/2}$ (lower panels), the inverse of the mass enhancement, largely follows T^* as expected. Increasing the doping density is expected to strengthen the Kondo effect since there are more conduction holes to screen the local moments; this is consistent with the observed dependence of T^* on ν_W.

Conclusion and Future Steps:

We have realized a Kondo lattice in AB-stacked $MoTe_2$/WSe_2 moiré bilayers. It opens exciting opportunities to study the gate-controlled Kondo destruction transition by extending the Kondo temperature further down to zero, for instance, by reducing the doping density in higher-quality devices or the interaction effect in small-twist-angle bilayers.

References:

[1] Kirchner, S., et al. Colloquium: Heavy-electron quantum criticality and single-particle spectroscopy. Rev. Mod. Phys. 92, 011002 (2020).

[2] Stewart, G. R. Heavy-fermion systems. Rev. Mod. Phys. 56, 755-787 (1984).

[3] Kumar, A., et al. Gate-tunable heavy fermion quantum criticality in a moiré Kondo lattice. Phys. Rev. B 106, L041116 (2022).

[4] Guerci, D., et al. Chiral Kondo lattice in doped $MoTe_2$/WSe_2 bilayers. Sci. Adv. 9. eade7701 (2023).

[5] Mak, K. F., and Shan, J. Semiconductor moiré materials. Nat. Nanotechnol. 17, 686-695 (2022).

Thin-Film Deposition for Surface Characterization Studies for Superconducting Radio Frequency Cavity Application

CNF Project Number: 2779-19
Principal Investigator(s): Matthias Liepe
User(s): Nathan Sitaraman, Sadie Seddon-Stettler

Affiliation(s): Cornell Laboratory for Accelerator-based Sciences and Education, Cornell University

Primary Source(s) of Research Funding: National Science Foundation under Award PHY-1549132, the Center for Bright Beams

Contact: mul2@cornell.edu, nss87@cornell.edu, sgs238@cornell.edu

Website(s): https://physics.cornell.edu/matthias-liepe

Primary CNF Tools Used: CVC SC4500 Combination Thermal/E-gun Evaporation System (Odd-Hour), AJA Sputter Deposition 1 & 2

Abstract:

Superconducting radio-frequency (SRF) cavities are a key component of particle accelerators (with applications ranging from fundamental physics research to synchrotron X-ray sources, to e-beam microscopy and lithography) and are also being developed for applications in dark matter detection and quantum computing. We are developing next-generation surface treatments to enhance the performance of niobium superconducting surfaces. By using facilities at the CNF, we investigate the effect of metallic doping on the niobium surface. We highlight our recent success in altering the niobium native oxide by zirconium doping and by gold doping.

Summary of Research:

We used CNF's AJA sputter deposition tools to deposit zirconium on niobium sample coupons. Prior to deposition, coupons received a standard pre-preparation consisting of a 60-micron electropolish, a 5-hour 800°C vacuum bake, and a 2-micron electropolish. The sputter deposition tool first removed the niobium native oxide by argon plasma sputtering, and then deposited approximately 2, 3.75, 7.5, and 10 nm of zirconium on four different samples. The deposition rate was based on the rate for similar metals and has not yet been directly calibrated. The samples then received another 800°C vacuum bake in order to fully dissolve any remaining niobium oxide and establish a uniform interface between the niobium metal and the protective zirconium oxide layer.

For increasing zirconium deposition thickness in the range of 0-3.75 nm, we find that the oxide rapidly becomes more zirconium-rich; in particular, by 3.75 nm thickness, there is no detectable niobium component in the primary oxide. Additionally, the combined intensity of the niobium and zirconium suboxide peaks decreases slightly relative to the intensity of the niobium metal peak, suggesting that the suboxide layer in the 2 nm and 3.75 nm samples is very thin. For increasing zirconium deposition thickness in the range 3.75-10 nm, however, both the primary ZrO_2 oxide and the suboxide become thicker.

We also used CNF's CVC SC4500 evaporation deposition system to deposit thin (1-2nm) layers of gold on niobium samples (prepared according to the standard pre-preparation in the earlier paragraph). This work recreated work done by a previous user from the group, Zeming Sun [1]. This work removed the oxide chemically with dilute hydrofluoric acid rather than argon plasma sputtering (as was used for zirconium deposition). We found substantial oxide still present, indicating opportunities for improvement of the process. However, we found some modification of the oxide, indicating that gold layers are promising towards oxide passivation.

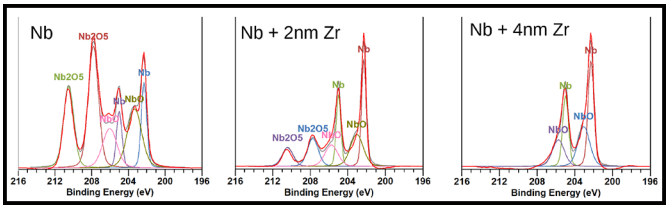

Figure 1: Peak fitting of niobium XPS data. The overallniobium oxide intensity decreases monotonically with increasing zirconium deposition thickness, and the pentoxide intensity in particular becomes undetectable by 3.75 nm zirconium deposition thickness. XPS sample analysis was performed at CCMR.

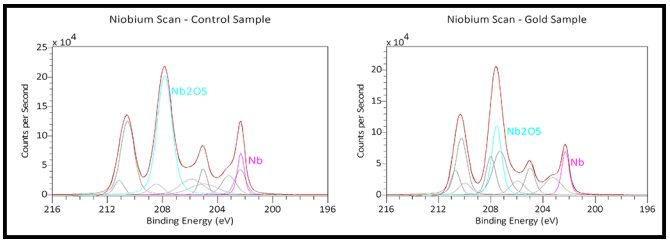

Figure 2: Preliminary peak fitting of niobium-gold XPS data. Control sample is bare niobium that has been exposed to atmosphere, gold sample has 1 nm of gold deposited on niobium. The oxide is still present, but has changed structure slightly. XPS sample analysis was performed at CCMR.

Conclusions and Future Steps:

We have demonstrated a method to eliminate the niobium pentoxide from a niobium superconducting surface. We expect that this method may be applicable to niobium superconducting devices and niobium-zirconium alloy surfaces, as well as possibly other niobium-based superconducting surfaces which typically form a niobium-rich oxide. We plan to investigate the effect of replacing niobium pentoxide with zirconium dioxide on SRF performance. We will also attempt to apply this method to the Nb_3Sn surface, and we will investigate other passive oxide layers such as hafnium, aluminum, and silicon oxide for SRF applications. We have also completed preliminary studies with thin-film depositions of gold, and will continue to investigate deposition methods to optimize the procedure for oxide passivation.

References:

[1] T. Oseroff, Z. Sun, and M. Liepe, "Measurements of the amplitude-dependent microwave surface resistance of a proximity-coupled Au/Nb bilayer," arXiv, 2023. doi:10.48550/arXiv.2305.12035.

Lithography for *in situ* Cryogenic Scanning Transmission Electron Microscopy

CNF Project Number: 2967-21
Principal Investigator(s): Jeeyoung Judy Cha
User(s): James L. Hart, Saif Siddique

Affiliation(s): Department of Materials Science and Engineering, Cornell University

Primary Source(s) of Research Funding: The Gordon and Betty Moore Foundation's EPiQS Initiative, Grant GBMF9062

Contact: jc476@cornell.edu, jlh487@cornell.edu, ms2895@cornell.edu

Website(s): cha.mse.cornell.edu

Primary CNF Tool Used: Nabity System for Supra SEM, PDMS Casting Station - Rm 224

Abstract:

Charge density waves (CDWs) of two-dimensional (2D) layered materials such as tantalum disulfide (TaS_2) and rare-earth tri-tellurides (RTe_3; R = rare-earth) can be used to make energy-efficient memory devices. To realize potential device applications, the CDW phase transitions of these materials should be studied at the nanoscale in the length scales of devices, and the changing transport properties must be correlated with the CDW phase transitions. In this project, we fabricate nanodevices of TaS_2 and RTe_3 on transmission electron microscopy (TEM) *in situ* chips such that we can operate the device inside a TEM, directly visualize the CDW phase transitions, and measure the transport properties during the CDW phase transition as a function of temperature between 100 K and 300 K.

Summary of Research:

We have successfully induced the CDW phase transitions of TaS_2 nanodevices during *in situ* cryo STEM experiments by both cooling down to 100 K (Figure 1) and by electric field. We have directly visualized the nucleation and growth of the nearly commensurate (NC) CDW out of the commensurate (C) CDW in TaS_2 nanodevices (Figure 2) and established that the nucleation of the NC-CDW state is defect-mediated (Figure 3). We have also proved that the electric-field induced phase transition from the C-CDW phase to the NC-CDW phase in TaS_2 is via Joule-heating, rather than strictly field-induced. We have also observed surprising CDW behaviors in exfoliated RTe_3 flakes due to stacking disorders present in these nanoscale samples.

Conclusions and Future Steps:

Our experiments constitute the first demonstrations of real-space direct imaging of electronic phase transitions in layered materials and the important role layer stacking disorders play on these electronic phase transitions. Three manuscripts are in preparation for submission this summer, which summarize our findings: (1) Defect-mediated CDW phase transition in TaS_2, (2) Field-induced CDW phase transition in TaS_2 is via Joule heating, and (3) Suppression of CDW phases in exfoliated RTe_3 flakes.

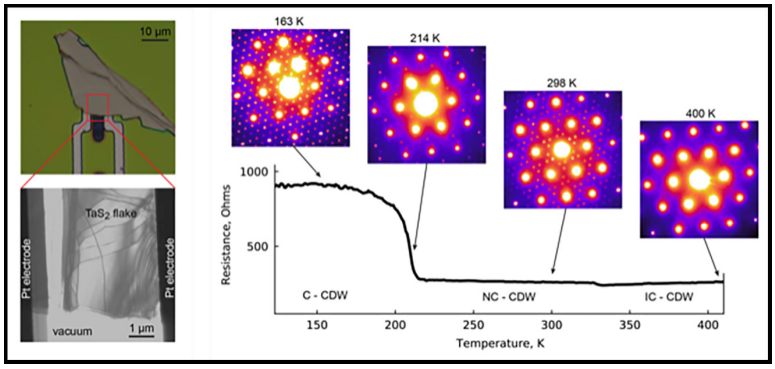

Figure 1: (Top, left) Optical micrograph of TaS_2 flake nanodevice with two electrodes. (Bottom, left) TEM image of the same TaS_2 flake, with stacking disorders shown as dark lines. (right) in situ *resistance measurement as well as* in situ *4D STEM acquisition of the TaS_2 nanodevice as a function of temperature down to 110 K. The C-CDW and NC-CDW phases can be distinguished by the superlattice patterns in the electron diffraction.*

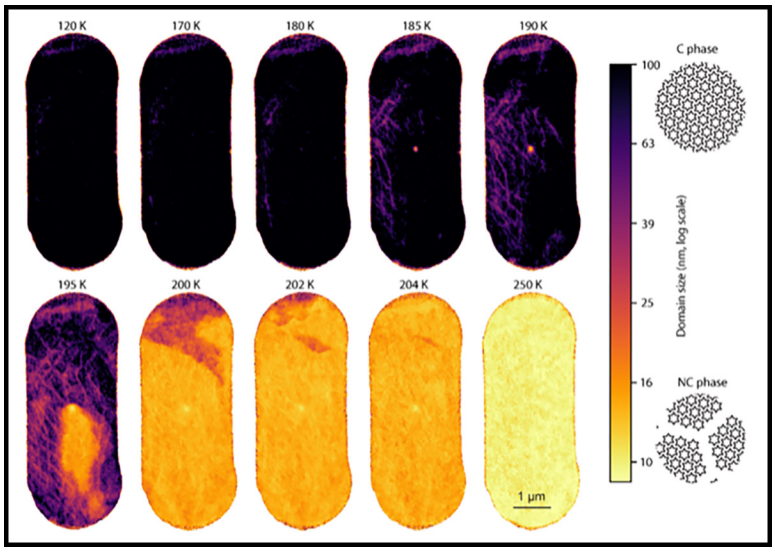

Figure 2: Nucleation and growth of the NC-CDW phase out of the C-CDW phase in the TaS_2 device as the temperature increases from 120 K to 250 K.

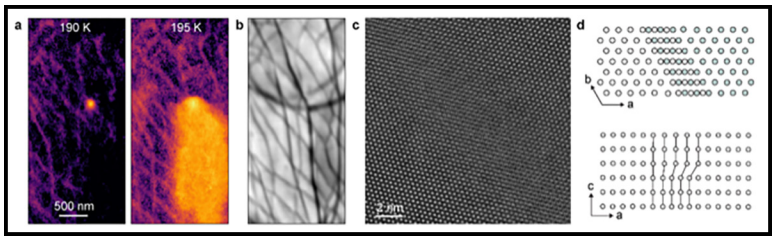

Figure 3: The nucleation of the NC-CDW phase (a) coincides with the location where the layer disorder defects (dark lines) merge (b). These dark lines were imaged in atomic resolution (c) to reveal the layer stacking disorder (d).

Novel Superconducting Microwave Devices from 2D Materials

CNF Project Number: 2998-22
Principal Investigator(s): Valla Fatemi
User(s): Luojia Zhang

Affiliation(s): Applied and Engineering Physics, Cornell University

Primary Source(s) of Research Funding: N.A (startup)

Contact: vf82@cornell.edu, lz282@cornell.edu

Primary CNF Tools Used: DWL66, DWL2000, PT770, ABM contact aligner, PT770, Nabity Nano Pattern Generating System, DISCO Dicing Saw, JEOL 6300, AJA Sputterer

Abstract:

We have made some decent progress in our nano-device fabrication within CNF this year. Our research has been focusing on measuring electronic transport properties of 2D materials Josephson junction, as well as high-Q microwave devices for qubit control / readout.

Summary of Research:

The first project was observing Josephson effect in junction made from hBN-graphene-hBN heterostructure. Although several groups have reported large Josephson supercurrent in such devices before, our device was the first successful graphene JJ fabricated completely within Cornell University. The accomplishment is from the success in the following fabrication process:

1. EBL: we performed electron-beam lithography to write the planar junction with 800 nm width and 5 μm length using the Nabity Nano Pattern Generating System (Figure 1. (a)).

2. Etching: we performed reactive ion etching using Oxford 81 to etch through the 2D materials stack and expose the graphene on the edge to form a one-dimensional contact with deposited metal (Figure 1. (b)).

3. Deposition: we have developed a good sputtering recipe for superconducting niobium which yielded 8.5K critical temperature (Figure 1. (c)).

We measured the device in a dilution refrigerator, and found a gate tunable Josephson supercurrent with maximum as large as 1.5 microamperes (Figure 1. (d)). The success of this device paved the way for the development of future more novel mesoscopic 2D materials devices.

Recently, we have fabricated a new batch of Josephson junction at CNF with bilayer graphene and WSe_2 to study the effect of spin-orbit coupling in the superconducting proximity effect.

The microwave devices we fabricated are the 2D transmission line resonators. We deposited a layer of 70 nm niobium using our sputtering recipe, then we performed photolithography on it with DWL66. We found that DWL66 is particularly useful for checking designs before finalizing them on a photomask, and handling features that are too large to be written by EBL. We first performed etching using AJA ion mill. Details of the small structures of the device are shown in Figure 2. (a) and (b). The device quality factor was measured to be around 50000. The resonance phase and magnitude of the resonator are shown in Figure 2. (d). In the second batch, we performed etching using PT770 reactive ion etcher. The quality factor was improved by a factor of 6 (more data are still being collected on these newer devices).

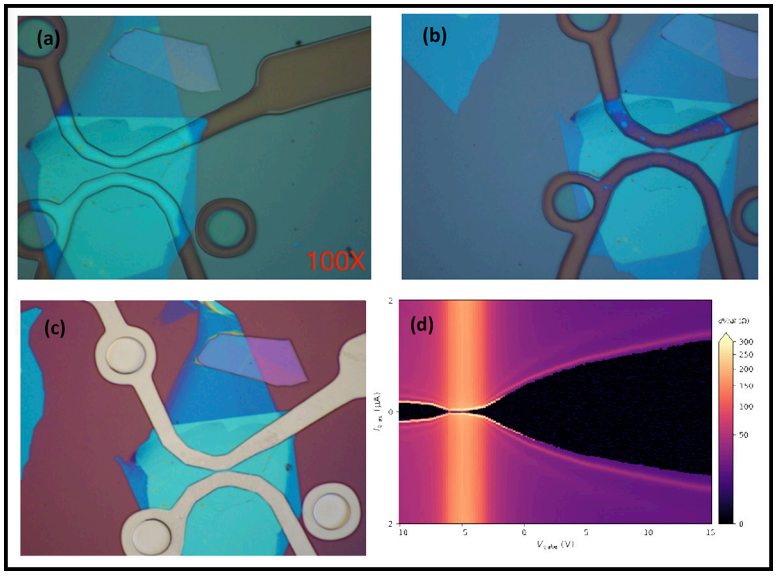

Manufacturing TiO_2 Pillar Arrays and SiN Bullseye Cavities

CNF Project Number: 3008-22
Principal Investigator(s): Professor Pablo A. Postigo
User(s): Christopher (Christer) Everly, Martin Sanchez

Affiliation(s): The Institute of Optics, University of Rochester

Primary Source(s) of Research Funding: UoR Startup

Contact: ppostigo@ur.rochester.edu, ceverly@ur.rochester.edu, msanch23@ur.rochester.edu

Website(s): https://www.postigolab.com

Primary CNF Tools Used: JEOL 6300, Spin Coaters, PT770 RIE, Microscopes, Oxford 82, Oxford 100, Plasma-Therm Tikachi HDP-CVD, Yes EcoClean Asher, Filmetrics systems, Zeiss Ultra SEM

Abstract:

Our group is interested in quantum research on photonic integrated circuit platforms. Two topics we are currently exploring are on-chip lasing, and single-photon emission enhancement with circular Bragg gratings. There have been recent reports of on-chip lasing achieved through bound states in the continuum. The bound states are made possible with an array of dielectric pillars. To study and reproduce these results we manufactured the same arrays at the Cornell NanoScale Facility.

Summary of Research:

This was the first time the user worked at CNF to create a nanostructure so we were mainly concerned with learning how to use the JEOL 6300, and to try a range of dosages to find the best parameters to create the nano pillars. We believe we found a good recipe for the electron beam exposure, but the reactive ion etching timing might need some tuning. Additionally, the quartz substrate we used was exceedingly thin — the vacuum chuck for the spin coater caused non-uniform coating to occur. Regardless, as seen from the images below we successfully created the pillar array.

Additionally, this was the first time the group was trying to manufacture bullseye cavities. Hence dosage tests and anisotropic reactive ion etch times are under study for this fabrication as well. RIE lag has caused an issue in etching smaller but important features in the bullseye cavities. It is still inconclusive as to if this problem will force us to use multiple exposures and etches to maintain the integrity of the smallest physical features.

Conclusions and Future Steps:

With the array of pillars manufactured, the next steps are to optically characterize. If the resonance is where we want it to be, then we proceed with coating the structure in CdZnS to further recreate the paper we are referencing.

For the bullseye cavities, more fabrications will be done to dial in on the best e-beam dosage and etch time. AFM images will be made to determine whether the central hole of the bullseye in future fabrications is up to spec with a single e-beam exposure and etch step, or if multiple exposure and etch steps need to be made to successfully create this bullseye cavity.

References:

[1] Room-Temperature Lasing in Colloidal Nanoplatelets via Mie-Resonant Bound States in the Continuum, Mengfei Wu, Son Tung Ha, Sushant Shendre, Emek G. Durmusoglu, Weon-Kyu Koh, Diego R. Abujetas, José A. Sánchez-Gil, Ramón Paniagua-Domínguez, Hilmi Volkan Demir, and Arseniy I. Kuznetsov; Nano Letters 2020 20 (8), 6005-6011, DOI: 10.1021/acs.nanolett.0c01975.

[2] Enhanced Emission from WSe_2 Monolayers Coupled to Circular Bragg Gratings, Ngoc My Hanh Duong, Zai-Quan Xu, Mehran Kianinia, Rongbin Su, Zhuojun Liu, Sejeong Kim, Carlo Bradac, Toan Trong Tran, Yi Wan, Lain-Jong Li, Alexander Solntsev, Jin Liu, and Igor Aharonovich; ACS Photonics 2018, 3950-3955, DOI: 10.1021/acsphotonics.8b00865.

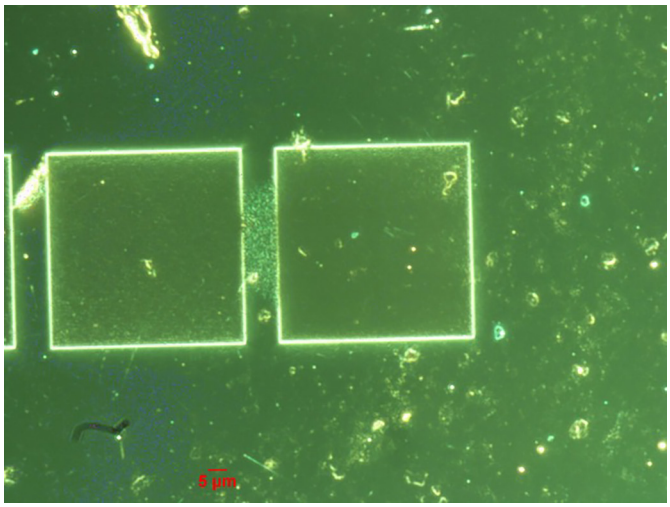

Figure 1: A microscope image of two pillar arrays made at CNF with the JEOL 6300.

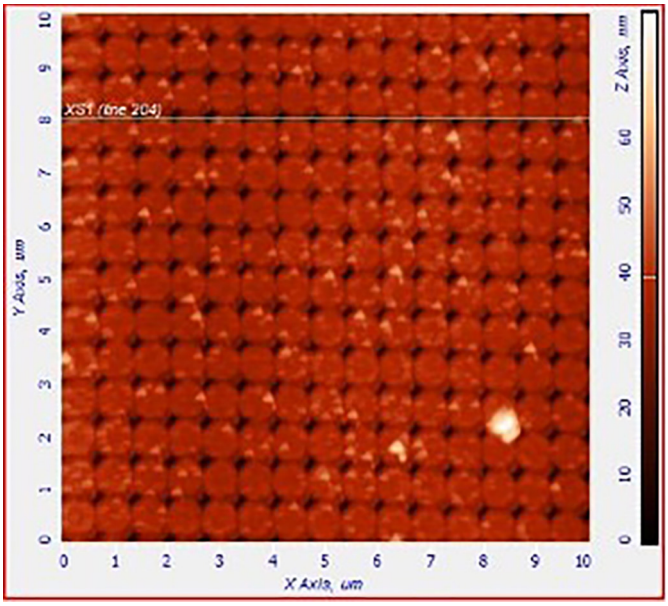

Figure 2: An Atomic Force Microscopy image of the array of pillars.

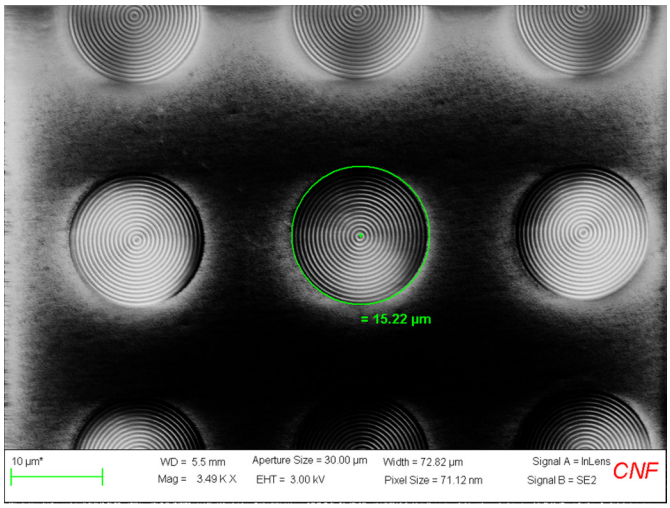

Figure 3: Array of bullseye cavities taken in Zeiss SEM Ultra.

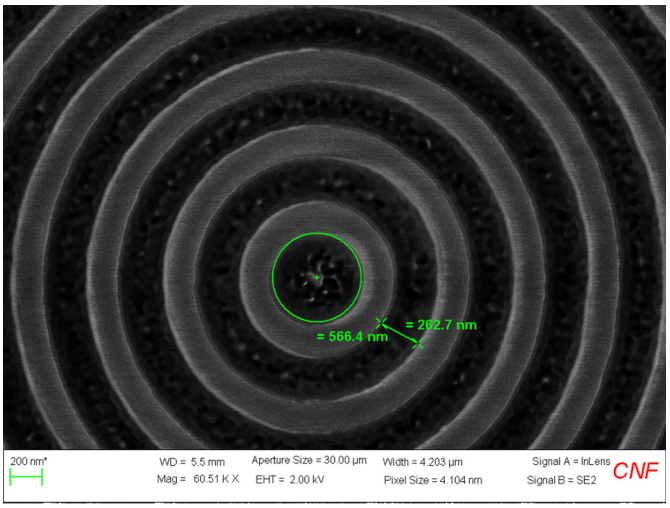

Figure 4: Center of bullseye cavity taken in Zeiss SEM Ultra.

Fabrication of Fluxonium-Like Qubits

CNF Project Number: 3010-22
Principal Investigator(s): Ivan Pechenezhskiy
User(s): Benjamin Byrd, Kesavan Manivannan

Affiliation(s): Department of Physics, Syracuse University

Primary Source(s) of Research Funding: Syracuse University, Army Research Office

Contact: ivpechen@syr.edu, babyrd@syr.edu, kmanivan@syr.edu

Primary CNF Tools Used: ASML DUV Stepper, JEOL 6300, PT770 Plasma Etcher, Heidelberg DWL2000 Mask Writer

Abstract:

In the drive for a scalable qubit-based processor, one of the most important resources is the ratio between qubit lifetime and gate operation time. Superconducting qubits provide a promising avenue for such a processor. Fluxonium qubits are exciting candidates in particular, having larger coherence times than the conventional transmons due to reduced sensitivity to several noise channels. Fluxonium qubits are intrinsically protected against charge noise due to the large inductive chain shunting the two capacitor pads, and protected against flux noise at the two flux sweet spots. Some of these qubits have lifetimes exceeding a millisecond, with gate times on the order of nanoseconds [1]. This project's fluxonium-like qubits are fabricated using an established recipe [2].

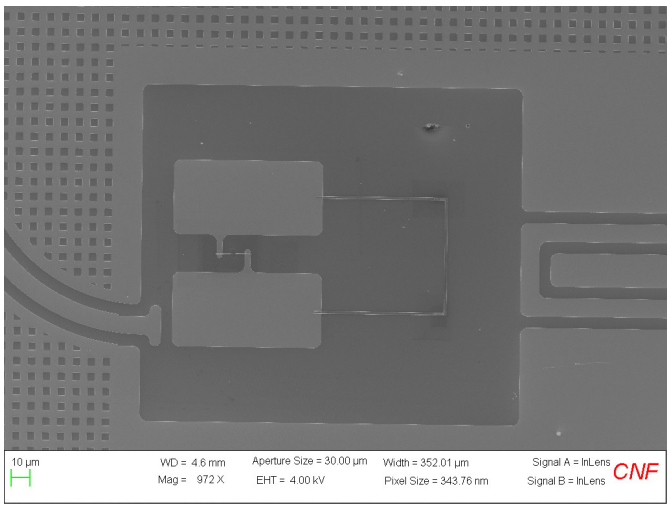

Figure 1: Scanning electron microscopy (SEM) image of one of the fluxonium qubits taken at CNF.

Summary of Research:

A fluxonium qubit is composed of a capacitive element, with a Josephson junction shorting the capacitive element. The key difference between a fluxonium and the more commonly studied transmon qubit is the inclusion of an inductor made of a chain of Josephson junctions, which shorts the two capacitor pads (Figure 1). This forms a closed loop for flux to thread through. This qubit is capacitively coupled to a resonator, whose frequency is shifted based on the state of the fluxonium qubit.

The devices are designed to facilitate direct control of each qubit on chip. For each device, there is one flux line per fluxonium and one charge bias line per transmon. These chips also utilize direct microwave drive lines to the individual qubits. Flux traps are etched across the entire ground plane of the chip, to limit the interaction of stray magnetic vortices with the fluxonium qubits. The resonant frequencies of the co-planar waveguide resonators on the chip are carefully chosen to ensure effective coupling with the qubits and easy measurement with the lab electronics. Test structures are distributed along the chip's edges, allowing for post-fabrication checks on the quality of electron-beam lithography and evaporation.

The fluxonium qubits are fabricated first by depositing a layer of niobium on a silicon wafer at Syracuse University using sputtering. The Heidelberg DWL2000 is used to construct a photomask equipped with various modular components to allow for tuning of circuit parameters after the design is finalized. Each of the chips is fabricated with two fluxonium and two transmon qubits. Frequencies for both of the qubits are targeted to be the same so that the properties of the two different qubit architectures can be compared. They are fabricated simultaneously on the same chip to reduce the factors related to fabrication variability.

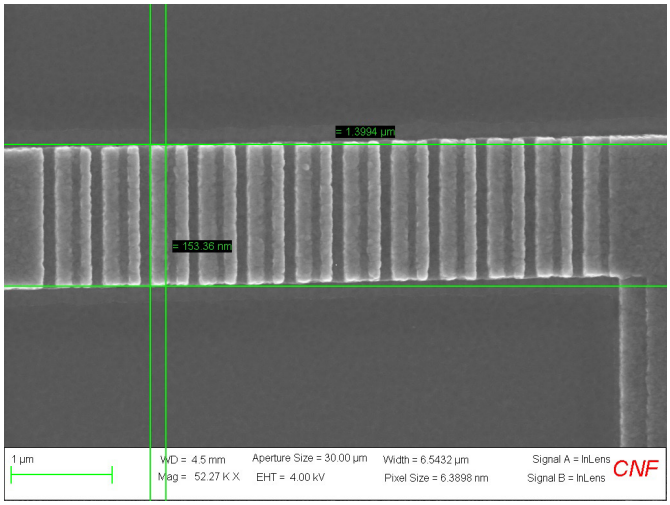

Figure 2: SEM image of a Josephson junction chain, taken at CNF.

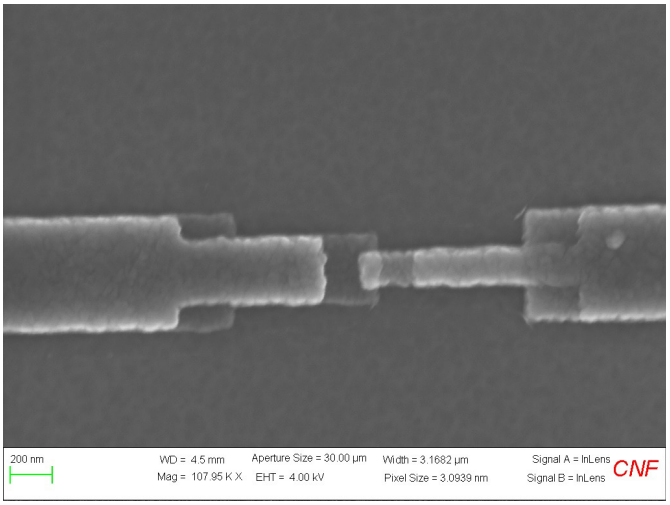

Figure 3: SEM of a single small Josephson junction, taken at CNF.

The base layer pattern (including the readout resonators, capacitor pads for the fluxonium and the transmon qubits, as well as the readout coplanar waveguide) is patterned into this niobium layer with the ASML DUV stepper. The wafer is then developed and cleaned before having the pattern etched into the superconducting niobium with the PT770. To remove oxides that may degrade the qubit performance, an additional HF cleaning step is done, after which the wafer is prepared for electron-beam lithography. After the electron-beam lithography pattern is developed, the device will have bridges formed of the remaining resist, which enables double-angle shadow evaporation for making the Josephson junctions. The lower pads for the Josephson junctions are deposited first, then the junctions are oxidized, and finally, the upper pads are deposited (Figure 2). This is all done with only a single electron-beam lithography.

The technique can be used to form the chain of Josephson junctions that serve a role of an inductor and the singular small junction (Figure 3). This evaporation and the intermediate oxidation are done at Syracuse University.

After the small junctions and the junction chain have been formed, the devices are returned to CNF to be diced. These devices are measured at Syracuse University in a Bluefors dilution refrigerator at temperatures below 10 mK.

The goal is to develop the capability to target specific qubit parameters and to optimize said parameters for a higher energy relaxation T1 and phase coherence T2 times. These devices also will benefit from expanding the range of fabrication techniques used in the fabrication process, potentially further limiting loss and increasing qubit lifetimes.

References:

[1] A. Somoroff, et al. Millisecond Coherence in a Superconducting Qubit. Phys. Rev. Lett., 130, 267001 (2023). https://doi.org/10.1103/PhysRevLett.130.267001.

[2] V. Iaia, et al. Phonon downconversion to suppress correlated errors in superconducting qubits. Nature Communications, 13, 6425 (2022). https://doi.org10.1038/s41467-022-33997-0.

Serpentine Heater Lines

CNF Project Number: 3016-22
Principal Investigator(s): Andrea Pickel
User(s): Benjamin Harrington, Kyle VanDelden, Jay VanDelden

Affiliation(s): Department of Mechanical Engineering, Materials Science Program, University of Rochester; EigenPhase Techologies

Primary Source(s) of Research Funding: National Science Foundation

Contact: apickel@ur.rochester.edu, bharrin9@ur.rochester.edu, kylevandelden@gmail.com, jvd@eigenphase.com
Website(s): https://labsites.rochester.edu/pickel/

Primary CNF Tools Used: Wire bonder, mask writer, ion mill, stepper, evaporator

Abstract:

Testing the performance of new nanoscale thermometry tools requires test structures that produce steep nanoscale temperature gradients. To achieve this outcome, we designed and fabricated Nichrome serpentine heater lines on crystalline quartz substrates that allow for four-point probe electrical measurements. When the serpentine lines are Joule heated, the current density concentrates at the inner corners of the heater lines. This results in a higher temperature rise at the inner corners than the outer corners, a geometric effect known as "current crowding" [1]. The low thermal conductivity of the Nichrome alloy helps maintain the temperature gradient between the inner and outer corners of the serpentines, while the use of the crystalline quartz substrate (factor of ~ 10 higher thermal conductivity than amorphous quartz) maintains the overall temperature rise at a reasonable level.

Summary of Research:

After first making a mask, the serpentine heater lines were then fabricated using a stepper lithography process. Individual chips containing an array of serpentine heater lines were created by dicing the crystalline quartz wafers on which the serpentine lines were fabricated (Figure 1).

Ultrasonic wire bonding was performed on the Westbond 7400A wire bonder at the Cornell NanoScale Facility. The goal was to electrically connect contacts on a printed circuit board (PCB) to the serpentine heater line chip. Over the course of the project, around 50 serpentine heater lines were attached to PCBs through silver epoxy at the University of Rochester (U of R) and brought to Cornell to be wire bonded. For each sample, four 1.25 mil aluminum wedge-to-wedge wire bonds were placed, corresponding to each of the gold contact pads on the PCB leading to the Nichrome pads on the serpentine heater line chip.

Once wire bonded, the heater line/PCB samples were brought back to the U of R to measure the resistance of serpentine heater line section only by means of a four-point probe resistance measurement. The sample was placed atop a hot plate and its resistance was monitored as the temperature increased. A temperature vs. resistance plot with an expected positive linear relationship was generated, and a temperature coefficient of resistance (TCR) value was calculated for the serpentine heater lines (Figure 2). The TCR value will serve as a calibration basis for later experiments, where the heater line will need to be held at a specific temperature via Joule heating.

Conclusions and Future Steps:

Nichrome serpentine heater lines on crystalline quartz substrates were successfully fabricated and the TCR value was calibrated. Major next steps are to measure the temperature rise as a function of the input Joule heating current and to subsequently use the Joule-heated serpentine lines to demonstrate nanoscale temperature mapping.

References:

[1] Q. Weng, et al., "Near-Field Radiative Nanothermal Imaging of Nonuniform Joule Heating in Narrow Metal Wires," Nano Letters 18, 7, 4220-4225 (2018).

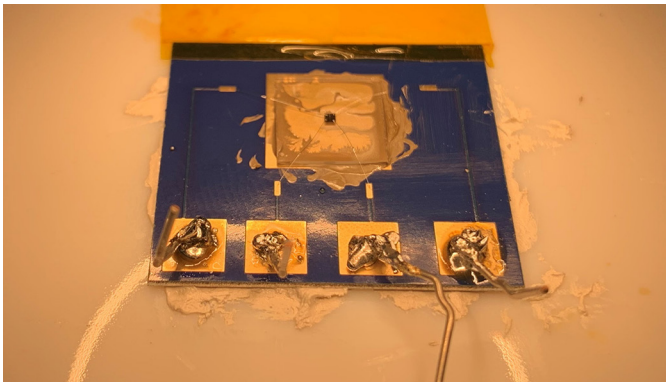

Figure 1: Wire bonded serpentine heater line and PCB sample. Wires soldered onto contact pads of the PCB are used for four-point probe measurements. Wire bonds connect the PCB to the serpentine heater line; in this setup the heater line chip has a single serpentine heater line. The bottom of the PCB is coated with thermal paste and is placed atop a hot plate.

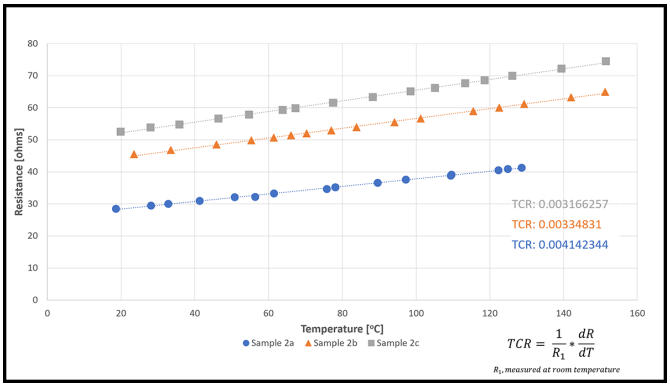

Figure 2: Temperature vs. resistance plot for Nichrome serpentine heater lines. Calculated temperature coefficient of resistance (TCR) values using the formula shown in the figure are also displayed for each respective sample.

Characterization of Fluxonium Qubits

CNF Project Number: 3067-23
Principal investigator(s): Ivan Pechenezhskiy
User(s): Benjamin Byrd, Kesavan Manivannan

Affiliation(s): Syracuse University
Primary CNF Tools Used: Army Research Office
Contact: ivpechen@syr.edu, babyrd@syr.edu, kmanivan@syr.edu
Primary CNF Tools Used: ASML DUV Stepper, JEOL 6300, PT770, Heidelberg Mask Writer - DWL2000

Abstract:

We fabricate and characterize superconducting fluxonium qubits made of nano-scale Josephson junctions as their primary element. Fluxonium qubits are one of the leading candidates for building scalable quantum computing processors owing to their very high (millisecond-long) characteristic times and large anharmonicity [1].

A more rigorous characterization and mitigation of the correlated noise channels affecting this class of qubits is required to further improve the qubit performance to a level where fault-tolerant processors can be built. We aim to study the different extrinsic and intrinsic decoherence mechanisms that couple to this superconducting qubit and attempt to mitigate them.

Summary of Research:

Superconducting quantum systems play a vital role in quantum computing. Superconducting qubits are lithographically defined devices in which the information is stored in quantum degrees of freedom of anharmonic oscillators. Josephson tunnel junctions provide the necessary anharmonicity. A fluxonium qubit has a small Josephson junction shunted by two large capacitor pads and a chain of Josephson junctions acting as a large inductor [2].

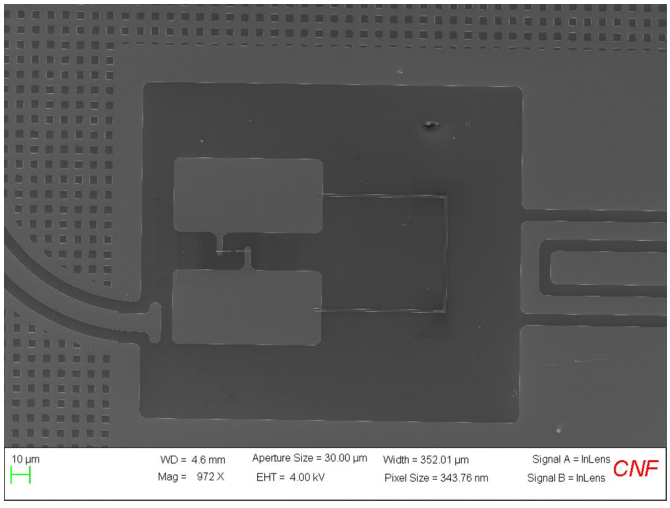

Figure 1: Scanning electron microscopy image of the fluxonium qubit showing the capacitor pad, single Josephson junction and the chain of Josephson junctions.

The flux bias through the formed loop can be tuned to vary the properties of this qubit. When a half-integer superconducting flux quantum threads the loop, the qubit exhibits a very high coherence and large anharmonicity.

The scanning electron microscopy image of our fluxonium qubit fabricated at CNF is displayed in Figure 1. The figure shows the two large niobium capacitor pads that set the capacitive energy scale $E_C/h \sim 1.4$ GHz. The small Josephson junction between the pads determines the Josephson energy $E_J/h \sim 2.3$ GHz. The array of 130 Josephson junctions to the immediate right of the pads is associated with the inductive energy $E_L/h \sim 0.5$ GHz. The capacitor pads are 40 μm × 80 μm in size and are patterned during the photolithography stage. The 90 nm × 100 nm Al-AlO_x-Al small junction and the array junctions, each of which have a dimension of 1.3 μm × 0.1 μm, are fabricated using the electron-beam lithography tool at CNF and electron-beam evaporator at Syracuse University. The Hamiltonian of the qubit can be tuned by modifying the properties of the above elements. The flux bias line can be seen on the right of Figure 1. Each qubit is capacitively coupled to a coplanar waveguide resonator, shown on the left of Figure 1, for dispersive readout of the qubit state.

The fabricated devices are cooled down to less than 10 mK for measurements. Microwave electronics at room temperature is used to manipulate and read out the qubit. Figure 2 shows the data from microwave transmission through a feedline coupled to the readout cavity as a function of flux bias through the loop. This flux-periodic feature is the tell-tale sign of the qubit ring being galvanically closed and the fabricated qubits fully functional. The qubit spectroscopy data in Figure 3 shows the two fundamental transitions, from the ground to the first excited state and from the ground to the second

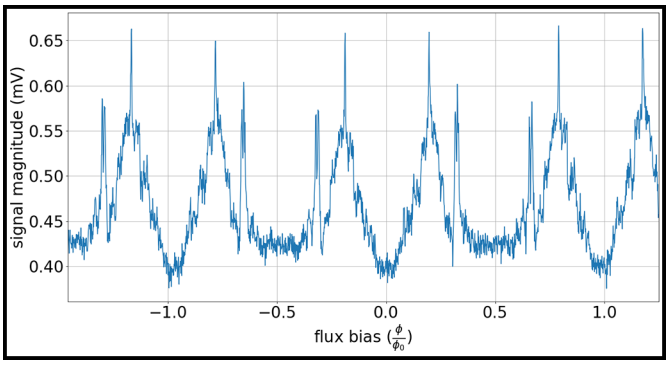

Figure 2: Flux-periodic transmission signal magnitude of the resonator coupled to the fluxonium qubit.

excited state, as a function of the flux through the loop. There is a reasonable agreement between the intended characteristic energy parameters and the ones obtained from fits to the spectrum showing the robustness of the fabrication procedure [3].

In the near future, going beyond the tune-up measurements, we would like to characterize the effect of decoherence due to injected quasiparticles in our fluxonium qubits.

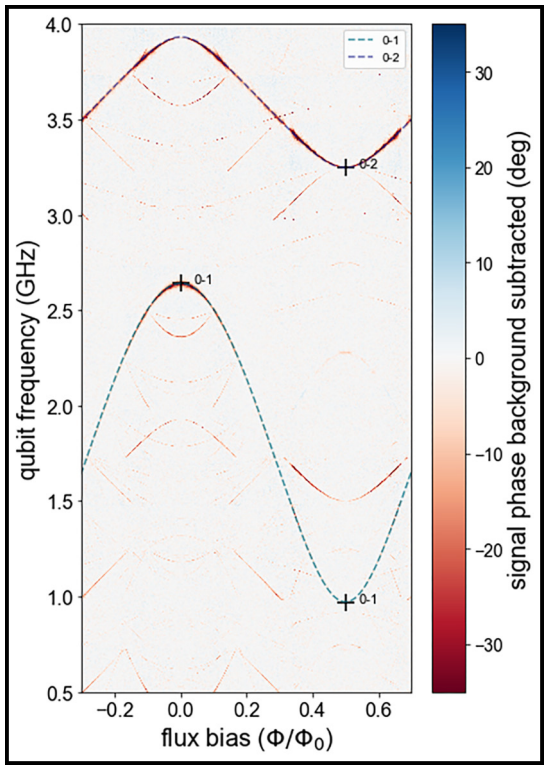

Figure 3: Fluxonium qubit spectrum showing the ground to the first excited and the ground to the second excited transitions.

References:

[1] A. Somoroff, et al. Millisecond Coherence in a Superconducting Qubit. Phys. Rev. Lett., 130, 267001 (2023). https://doi.org/10.1103/PhysRevLett.130.267001.

[2] L. Nguyen, et al. High-Coherence Fluxonium Qubit. Phys. Rev. X, 9, 041041 (2019). https://doi.org/10.1103/PhysRevX.9.041041.

[3] V. Iaia, et al. Phonon downconversion to suppress correlated errors in superconducting qubits. Nature Communications, 13, 6425 (2022). https://doi.org10.1038/s41467-022-33997-0.

Nanoscribe Advanced Patterning Techniques for Two-Photon 2D and 3D Structures

2023 CNF REU Intern: Samantha Averitt
Intern Affiliation: Mechanical Engineering, University of California Berkeley

CNF REU Mentors: Roberto Panepucci, Giovanni Sartorello; Cornell NanoScale Facility Staff, Cornell University

Program & Primary Source of Research Funding: 2023 Cornell NanoScale Science & Technology Facility Research Experiences for Undergraduates (CNF REU) Program via the NSF under Grant No. NNCI-2025233

Contact: saveritt@berkeley.edu, rrp23@cornell.edu, gs664@cornell.edu

Website: https://cnf.cornell.edu/education/reu/2023

Primary CNF Tools Used: Nanoscribe GT2, Zeiss Supra SEM, Glen 1000 Resist Strip

Abstract:

The CNF's Nanoscribe GT2 is a laser lithography system capable of printing three-dimensional structures with a resolution down to 200 nm using two-photon polymerization (2PP). Whereas traditional 2D direct writing (DW) tools require 3D structures to be built up one layer at a time, the Nanoscribe allows for complex 3D geometries to be fabricated with multiple levels in a single process step. Moreover, due to its high resolution, extending this tool to the fabrication of 2D structures provides researchers with enhanced flexibility for their process flows. In this work, we explore the Nanoscribe's capabilities in various configurations, with an emphasis placed on process development for spin-coated resists. An alignment strategy is demonstrated, enabling structures to be printed with overlay accuracy of approximately one micron using pre-existing fiducial markers. By investigating the capabilities of this tool, we also gauge its ability to aid in processes such as lift-off and microfluidic mold fabrication, potentially enabling the realization of devices that would be difficult to create using other methods.

Summary of Research:

To test the resolution capabilities of this tool, oil immersion was used due to oil having a higher index of refraction compared to air, increasing the objective's numerical aperture. Resolution tests were conducted on S1813 and SU-8, using computer-aided design (CAD) with both horizontal and vertical lines of widths ranging from 0.2 to 4 μm. Line widths under 340 nm were observed for the 200 nm nominal CAD on S1813 at a scan speed of 1000 μm/s and a laser power of 10% (Figure 1). Larger line widths of ~ 700 nm were observed for SU-8 at a scan speed of 500 μm/s and a laser power of 60%. We believe this was due to the higher dose required to ensure adhesion between the print and substrate post-development. Focusing was also an issue when working with non-standard materials, as Nanoscribe's automatic interface finding procedure was not possible in certain configurations.

The alignment capabilities of this tool were also investigated. Our proposed alignment strategy consists of two main components: a coordinate transformation followed by offset compensation.

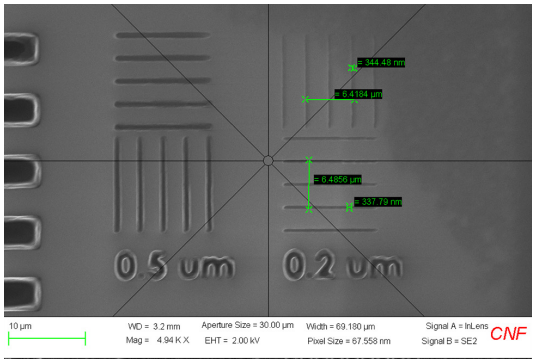

Figure 1: SEM of an S1813 oil immersion resolution test at a 1000 µm/s write speed and 10% laser power.

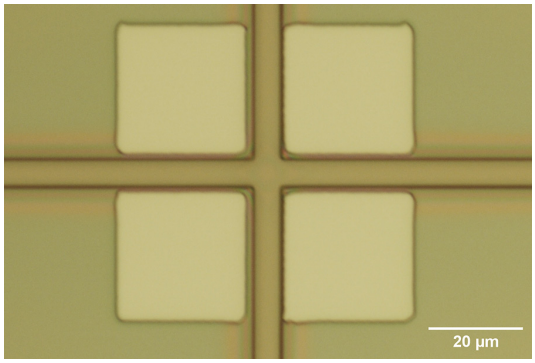

Figure 2: Optical microscopy image of an aligned print conducted using the 10x objective on S1813.

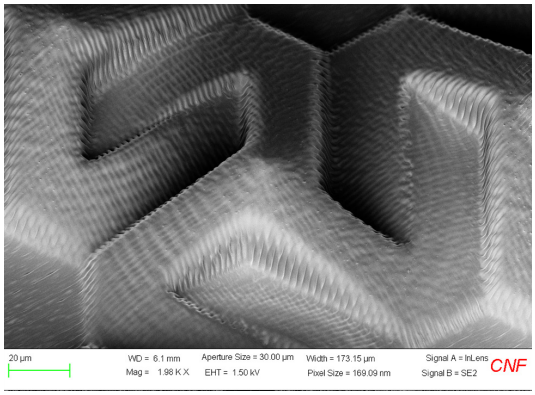

Figure 3: SEM of grayscale print conducted using the 10x objective with IP-Q and slicing distance of 1 µm.

First, a coordinate transformation is performed by the user with alignment to pre-existing marks. This enables stage movement to known locations on the substrate.

Second, offset compensation is required to account for the offset between the camera and laser system. This is done by opening the laser shutter until visible polymerization occurs, manually measuring the observed offset, and adjusting the system's stage position accordingly. It is important to note that this position varies depending on the objective being used. Following this procedure, we were able to demonstrate aligned prints with an accuracy of ~ 1 μm (Figure 2).

After investigating these capabilities, we explored potential applications of the Nanoscribe. Notable difficulties were encountered when exploring the direct fabrication of microfluidic devices on spin-coated resists. Experiments were conducted using both negative (SU-8) and positive (AZ4903) resists. Unfortunately, Nanoscribe's recommended AZ resins are no longer available. Using these resists, we saw incomplete channel development and long print times due to the slow write speeds required for exposure. Moving forward, alternative resins should be explored to address this problem.

We were able to successfully demonstrate the 3D capabilities of this tool through the creation of grayscale structures. Tests were conducted using both the 63x objective with S1827 and the 10x objective with Nanoscribe's IP-Q resin. Using the latter configuration, we observed adhesion issues when printing on bare silicon. This was resolved using plasma etching followed by the addition of a thin SU-8 adhesion layer. The effect of different print parameters was also investigated. We found that increasing the *FindInterfaceAt* value and dose delivered to the resin also helped to improve adhesion. Moreover, by decreasing the slicing distance parameter, we were able to demonstrate the ability of this tool to create 3D structures with relatively smooth surface profiles (Figure 3).

Additionally, we demonstrated the Nanoscribe's ability to be used in lift-off processes. Tests were conducted using the 10x objective on S1813 on LOR, with lift-off successfully occurring following the evaporation of gold and chromium on our sample. This process was performed in conjunction with our aforementioned alignment procedure.

We also conducted aligned prints on ultra-small pieces, approximately 1 mm^2 in dimension. These pieces were secured to a silicon substrate using polymethyl methacrylate (PMMA) before being immersed in IP-Q resin. From here, prints were aligned to the center of pre-existing circles and conducted using the 10x objective.

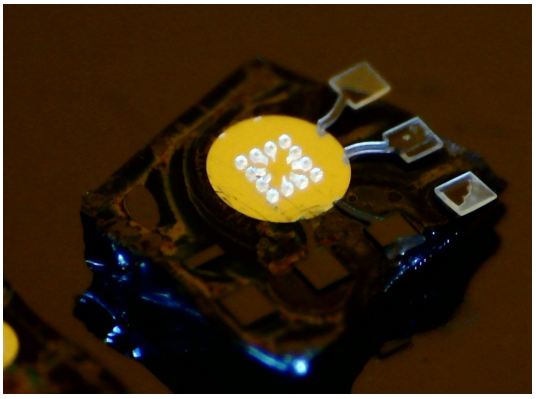

Figure 4: Image of an aligned print conducted using the 10x objective with IP-Q on a ~ 1 mm^2 piece.

The structures printed were 40 μm tall, and show the potential for this tool to create suspended geometries (Figure 4).

Conclusions and Future Steps:

Overall, this work demonstrates that Nanoscribe GT2 is a competitive tool for DW. Although larger than the 200 nm theoretical limit, the resolution results of this work remain non-trivial in showing this tool's capabilities. The linewidths observed are smaller than what is achievable with other DW methods at the CNF and could likely be decreased with additional parameter optimization. Moreover, in combination with its alignment capabilities, this tool has the potential to be used in a variety of applications from grayscale images, to lift-off, to direct fabrication on CMOS chiplets.

More process development is required regarding the Nanoscribe's ability to be used with other spin-coated resists. This, in combination with further parameter optimization, could further push the resolution limit of this tool. Additionally, quantitative characterization of this tool's alignment is still needed.

Acknowledgements:

Special thanks to the Cornell NanoScale Science & Technology Facility Research Experiences for Undergraduates (CNF REU) Program for hosting this internship and to the CNF staff for their support and mentorship. This work was funded by the National Science Foundation via grant no. NNCI-2025233.

References:

[1] NanoGuide Professional Photonic Series. (n.d.). Retrieved June 20, 2023, from https://support.nanoscribe.com/hc/en-gb/categories/201695349